

MULTIRESOLUTION BASED ON WEIGHTED AVERAGES OF THE HAT FUNCTION II: NONLINEAR RECONSTRUCTION TECHNIQUES*

FRANCESC ARÀNDIGA[†], ROSA DONAT[‡], AND AMI HARTEN[§]

Abstract. In this paper we describe and analyze a class of nonlinear multiresolution schemes for the multiresolution setting which corresponds to discretization by local averages with respect to the hat function. These schemes are based on the essentially-non-oscillatory (ENO) interpolatory procedure described in [A. Harten, B. Engquist, S. Osher, and S. Chakravarty, *J. Comput. Phys.*, 71 (1987), pp. 231–302]. We show that by allowing the approximation to fit the local nature of the data, one can improve the compression capabilities of the multiresolution algorithms. The question of stability for nonlinear (data-dependent) reconstruction techniques is also addressed.

Key words. multiresolution, adaptive stencils, subcell resolution

AMS subject classifications. 41A05, 41A15, 65O15

PII. S1064827596308822

1. Introduction. Fourier analysis provides a way to represent square-integrable functions in terms of their sinusoidal scale-components. Fourier decomposition techniques have become basic tools for a great variety of applications in many fields of science. However, there is a drawback that renders the Fourier decomposition of an *irregular* function practically useless: It is a global decomposition; an isolated singularity dominates the behavior of all coefficients in the decomposition and prevents us from getting immediate information about the function away from the singularity.

Local-scale decompositions fare much better in this respect. Typically, one starts with a finite sequence that is somehow associated with discrete information of a given signal at the finest resolution level considered. By processing the signal at different resolution levels, one can rewrite this discrete information in a new way. The new sequence has the same cardinality as the old one (if a nonredundant scheme is used) and its coefficients represent the details at each resolution level and a final coarse approximation to the original signal.

Multiresolution representations of $L^2(R)$ functions can be computed by decomposing the signal using a wavelet orthonormal basis. In the wavelet framework, all is done by a succession of orthogonal basis transformations; therefore, the inverse operation, i.e., recovering the incoming discrete signal from its multiresolution representation, is given by the adjoint matrices.

Wavelet orthonormal bases are composed of dilates and translates of a single function, the wavelet. The wavelet is intimately linked to the *scaling* function, sometimes called the *mother* wavelet. This function satisfies a dilation relation which is

*Received by the editors September 3, 1996; accepted for publication (in revised form) January 16, 1998; published electronically January 29, 1999.

<http://www.siam.org/journals/sisc/20-3/30882.html>

[†]Departament de Matemàtica Aplicada, Universitat de València, Spain (arandiga@godela.matapl.uv.es). The research of this author was supported in part by DGICYT PB94-0987 and ONR-N00014-95-1-0272.

[‡]Departament de Matemàtica Aplicada, Universitat de València, Spain (donat@rocafort.matapl.uv.es). The research of this author was supported in part by DGICYT PB94-0987, a grant from the Generalitat Valenciana, and ONR-N00014-95-1-0272.

[§]The author is deceased. Former addresses: School of Mathematical Sciences, Tel Aviv University, Tel Aviv, Israel; Department of Mathematics, UCLA, Los Angeles, CA 90024-1555.

in fact responsible for the properties of the multiscale decomposition. The construction of multiresolution schemes based on an orthonormal wavelet basis then becomes equivalent to a search for solutions in $L^2(R)$ of very particular dilation relations.

In [7, 8, 9] Harten develops a general framework for multiresolution representation of data. In his general framework, Harten abandons the dilation relation as the basic design tool and considers instead two operators, decimation and prediction, as the building blocks of a multiresolution scheme.

Let us consider a sequence of grids X_k corresponding (as k increases) to increasing resolution levels. The decimation operator, D_k^{k-1} , is a linear operator that yields the discrete information contents of the signal at the resolution $k-1$ from the discrete information at level k . The prediction operator, P_{k-1}^k , yields an approximation to the discrete information contents at the k th level from the discrete information contents at level $k-1$. Thus

$$(1.1) \quad \begin{aligned} (a) \quad D_k^{k-1} &: V^k \rightarrow V^{k-1}, \quad D_k^{k-1} \text{ a linear operator,} \\ (b) \quad P_{k-1}^k &: V^{k-1} \rightarrow V^k, \end{aligned}$$

where V^k is a space with a denumerable basis which is related to the level of resolution specified by X_k (for example, in many one-dimensional applications $V^k = S^k$, a space of sequences of dimension related to that of the grid X_k).

The basic property that these two operators have to satisfy is

$$(1.2) \quad D_k^{k-1} \cdot P_{k-1}^k = I_{k-1}, \quad \text{where } I_{k-1} \text{ is the identity operator in } V^{k-1},$$

which is nothing but a consistency relation: Predicted values at the k th resolution level should have the same information contents as the original values, when restricted to the $(k-1)$ st level. In addition, it is also required that D_k^{k-1} be onto. This requirement is also quite natural. It means that discrete information at each resolution level can always be thought of as the restriction (a term which is borrowed from the multigrid terminology) of some discrete information at the next resolution level.

A sequence of decimation and prediction operators $\{D_k^{k-1}\}$ and $\{P_{k-1}^k\}$ satisfying (1.1) and (1.2) define a multiresolution transform, i.e., a (one-to-one) correspondence between the original data and a multiscale decomposition of it. The inverse multiresolution transform allows us to recover the original (discrete) data from their multiresolution representation.

The direct and inverse multiresolution transforms are described algorithmically as follows: $v^L \rightarrow Mv^L$ (Encoding)

$$(1.3) \quad \begin{array}{l} \textbf{for} \quad k = L, \dots, 1 \\ \quad v^{k-1} = D_k^{k-1} v^k \\ \quad d^k = G_k(v^k - P_{k-1}^k v^{k-1}) \\ \textbf{end} \\ Mv^L = \{v^0, d^1, \dots, d^L\} \end{array}$$

$$Mv^L \rightarrow M^{-1}Mv^L \quad (\text{Decoding})$$

$$(1.4) \quad \begin{array}{l} \textbf{for} \quad k = 1, \dots, L \\ \quad v^k = P_{k-1}^k v^{k-1} + E_k d^k \\ \textbf{end} \end{array}$$

The multiresolution transform of v^L is composed of a low-level representation, that is, v^0 , and the *scale coefficients*, d^k , which are obtained from the prediction errors

$$e^k = v^k - P_{k-1}^k v^{k-1}$$

by removing the redundant information in them. Since $D_k^{k-1} e^k = D_k^{k-1} (v^k - P_{k-1}^k v^{k-1}) = 0$, e^k belongs to the null space of the decimation operator

$$e^k \in \mathcal{N}(D_k^{k-1}) = \{v \mid v \in V^k, \quad D_k^{k-1} v = 0\}.$$

Let us assume that $\dim V^k = N_k$. Then $\dim \mathcal{N}(D_k^{k-1}) = N_k - N_{k-1}$. Now let us select a set of basis functions in $\mathcal{N}(D_k^{k-1})$:

$$\mathcal{N}(D_k^{k-1}) = \text{span}\{\mu_j^k\}_{j=1}^{N_k - N_{k-1}}.$$

The operator G_k computes the coefficients of the prediction error in the basis $\{\mu_j^k\}$:

$$e^k = \sum_{j=1}^{N_k - N_{k-1}} d_j^k \mu_j^k, \quad d^k = G_k e^k.$$

The operator E_k simply computes a prediction error knowing the scale coefficients, i.e.,

$$E_k d^k = \sum_{j=1}^{N_k - N_{k-1}} d_j^k \mu_j^k \in \mathcal{N}(D_k^{k-1}).$$

Observe that $E_k G_k$ is the identity operator in $\mathcal{N}(D_k^{k-1})$.

It is easy to prove that there is a one-to-one correspondence between v^k and $\{d^k, v^{k-1}\}$, which implies in turn

$$v^L \xleftrightarrow{1:1} \{v^0, d^1, \dots, d^L\} = M v^L.$$

In electrical engineering terms, the basic encoding and decoding steps embodied in algorithms (1.3) and (1.4) are the analysis and synthesis steps of a subband filtering scheme with exact reconstruction. The operator D_k^{k-1} plays the role of a low-pass filter and the operator $G_k(I_k - P_{k-1}^k D_k^{k-1})$ that of a band-pass filter. Usually, these filters are linear and of convolution type (this is exactly the situation within the wavelet framework).

Of course, the whole purpose of subband filtering is not just to decompose and reconstruct. The goal of the game is to do some compression or processing between the decomposition and reconstruction stages. In this respect, Harten's framework is far more flexible than the wavelet framework. The prediction operator is not required to be linear; therefore it is possible to obtain adaptive (data-dependent) multiresolution representations which fit the approximation to the local nature of the data. On the other hand, the only adaptivity which is possible within the theory of wavelets is through redundant "dictionaries."

In Harten's framework, the design of a multiresolution scheme is directly related to the choice of sequences of decimation and prediction operators, subject to (1.1) and (1.2). The construction of these sequences depends on two fundamental tools:

discretization and reconstruction. The discretization operator obtains discrete information from a (nondiscrete) signal at a particular resolution level. The reconstruction operator produces an approximation of that signal from the discrete values.

Let \mathcal{F} be the space of functions to be subjected to a discretization process \mathcal{D} , which yields discrete information at the resolution level specified by the grid X . Then

$$\mathcal{D} : \mathcal{F} \longrightarrow V = \mathcal{D}(\mathcal{F}), \quad \mathcal{R} : V \longrightarrow \mathcal{F}.$$

We require that \mathcal{D} be a linear operator (it is onto by construction).

The function $\mathcal{R}\mathcal{D}f$ is regarded as an approximation to f , in the same function space to which f belongs. A basic consistency requirement is that the reconstruction from a set of discrete data must contain exactly the same discrete information, at the specified resolution level, as the original sequence. This can be expressed as follows:

$$(1.5) \quad \mathcal{D}\mathcal{R}v = v \quad \forall v \in V \quad \equiv \quad \mathcal{D}\mathcal{R} = I_V.$$

A sequence of discretization $\{\mathcal{D}_k\}$ can be used to define a family of decimation operators $\{D_k^{k-1}\}$. In order for this to happen, the sequence of discretization operators has to be *nested*. In plain language, the nested property implies that lower resolution levels contain no more discrete information than higher resolution levels. In mathematical terms this is expressed as follows:

$$(1.6) \quad \mathcal{D}_k f = 0 \quad \Rightarrow \quad \mathcal{D}_{k-1} f = 0.$$

Each decimation operator is then defined as follows: For any $v^k \in V^k$, let $f \in \mathcal{F}$ be such that $\mathcal{D}_k f = v^k$; then $D_k^{k-1} v^k = \mathcal{D}_{k-1} f$. The nested property implies that the definition is independent of f . Moreover, since \mathcal{D}_k is onto, we can write

$$D_k^{k-1} \mathcal{D}_k = \mathcal{D}_{k-1}.$$

It is easy to see that this definition satisfies the properties required of a decimation operator. We would also like to stress that, in practice, the decimation step is carried out without explicit knowledge of f .

Discrete data are usually obtained from a particular discretization process. This implies that very often the *nature* of the discrete data (i.e., the way in which they were generated) dictates the appropriate multiresolution setting in which these data should be analyzed. The goal in Harten's framework is the design of multiresolution schemes that apply to all sequences but that are particularly adequate for those obtained by the discretization process used to define the scheme.

The prediction operators are obtained from the sequences $\{\mathcal{D}_k\}$ and $\{\mathcal{R}_k\}$ as follows:

$$(1.7) \quad P_{k-1}^k v^{k-1} = \mathcal{D}_k \mathcal{R}_{k-1} v^{k-1};$$

then

$$D_k^{k-1} P_{k-1}^k v^{k-1} = D_k^{k-1} \mathcal{D}_k \mathcal{R}_{k-1} v^{k-1} = \mathcal{D}_{k-1} \mathcal{R}_{k-1} v^{k-1} = v^{k-1}$$

and (1.2) is satisfied.

One of the main concerns in the design of a multiresolution scheme is the *quality* of the prediction. The notion of k th scale is related to the information in v^k which cannot be predicted from v^{k-1} by *any* prediction scheme. When using a particular one,

the prediction errors, and consequently the scale coefficients d^k , include a component of approximation error which is related to the *quality* or *accuracy* of the particular prediction we used.

By expressing the multiresolution scheme in terms of a sequence of discretization and reconstruction operators, the problem of finding a suitable prediction operator for a multiresolution setting can be reduced to a typical problem in approximation theory:

Knowing $\mathcal{D}_{k-1}f$, $f \in \mathcal{F}$, find a “good approximation” to $\mathcal{D}_k f$.

The relation between the prediction operator and the reconstruction procedure opens up a tremendous number of possibilities for the design of multiresolution schemes, where the primary consideration is the selection of the appropriate discretization. We can consider not only linear reconstruction procedures, as in most wavelet-type multiresolution algorithms, but also nonlinear (data-dependent) reconstruction procedures.

Linear multiresolution schemes within Harten’s framework have been widely studied in [8, 9, 10] and [2]. In this series of works it is shown that biorthogonal wavelets can be thought of as the “uniform constant coefficient” case of the general framework. It corresponds to a choice of some weighted-average discretization in the real line together with a particular reconstruction procedure, which is in fact the natural one from the functional analysis point of view ($\mathcal{R}_k \mathcal{D}_k$ is a projection). Orthogonal wavelets are also obtained from Harten’s framework by imposing an additional constraint: the discretization and reconstruction operators are based on the *same* weight-function.

There is now a variety of data-dependent approximation techniques (e.g., the essentially-non-oscillatory (ENO) interpolatory technique of [12]) which are designed to minimize regions of low accuracy in the reconstruction when isolated singularities occur. When dealing with “irregular” signals, adaptive reconstruction techniques can reduce the approximation error component in d_j^k , leading to better compression rates than their linear counterparts.

In this paper we shall describe and analyze a class of nonlinear multiresolution schemes for the hat-average multiresolution setting. These schemes are based on the ENO interpolatory procedure described in [12].

The paper is organized as follows. The class of nonlinear reconstruction techniques we use as design tools is described in section 2, where we briefly review the ENO interpolatory procedure and Harten’s subcell-resolution (SR) technique.

In section 3 we review some basic results, obtained in [2], about the hat-average multiresolution setting and we set the notation for the remainder of the paper. The ENO-reconstruction with SR technique for the hat-average multiresolution framework is described in section 4. Special attention is paid, in section 5, to the application of the SR technique to *weak* singularities.

The stability theory developed in [9] does not apply to nonlinear prediction operators. The question of stability for the nonlinear multiresolution schemes we design is considered in section 6.

In section 7 we show several numerical experiments with comparisons, and finally some conclusions are drawn in section 8.

2. Nonlinear reconstruction techniques. The scale coefficients are directly related to the prediction errors, which measure our success in using the reconstruction procedure to climb up the ladder from low-resolution to high-resolution levels.

If $p \in \mathcal{F}$ is a function for which \mathcal{R}_{k-1} is exact, i.e.,

$$\mathcal{R}_{k-1}(\mathcal{D}_{k-1}p) = p$$

we have likewise

$$P_{k-1}^k(\mathcal{D}_{k-1}p) = \mathcal{D}_k \mathcal{R}_{k-1} \mathcal{D}_{k-1}p = \mathcal{D}_k p,$$

i.e., the prediction P_{k-1}^k is also exact on the discrete values associated to the function p . The quality, or accuracy, of the prediction can thus be judged by the class of functions in \mathcal{F} for which the reconstruction from their discrete values is exact.

If the set of exactness for the reconstruction operators includes all polynomials of degree $p-1$, typically one has also

$$(2.1) \quad \mathcal{R}_k \bar{f}^k(x) = f(x) + O(h_k^p)$$

in regions where $f(x)$ is smooth. We say then that the reconstruction operator is of *order* p . The accuracy of the reconstruction technique plays a key role in the efficiency of data compression algorithms of the types (1.3) and (1.4).

An isolated singularity affects the accuracy of the reconstruction in a region whose extent depends heavily on the type of the reconstruction procedure. For example, the effect of a discontinuity is felt everywhere (to a greater or lesser degree) when using a truncated Fourier series.

In [7, 8, 9] and [2] many of the reconstruction procedures considered are based on piecewise polynomial interpolation techniques. For these, the extent of the low accuracy region around a singularity depends on the stencil of points used to construct the polynomial pieces. It is clear that whenever the stencil crosses the singularity, (2.1) fails to hold.

Data-independent (linear) interpolatory techniques use a fixed stencil to construct each polynomial piece. Since the number of points in the stencil increases with polynomial degree (order of the interpolation), so does the extent of the low accuracy region.

In [12], Harten et al. introduce a data-dependent piecewise-polynomial interpolation technique which they refer to as ENO interpolation. The basic idea of the ENO technique is to enlarge the region of high accuracy by constructing the piecewise polynomial interpolants using only information from regions of smoothness of the interpolated function.

For piecewise smooth signals with a finite number of singularities, adaptive data-dependent reconstructions of order p manage to keep relation (2.1) valid over a larger region than linear (= data-independent) reconstructions of the same order. This implies that the approximation error component in the scale coefficients is smaller, thus leading to schemes with better compression properties.

Data compression algorithms based on cell-averaged multiresolution and ENO reconstructions applied to discontinuous piecewise smooth signals give much better compression rates than the corresponding algorithms with linear reconstructions (see [7, 10, 5]). Moreover, Harten shows in [7, 10] that the cell-average discretization enables us to get a good approximation even in cells which contain a jump discontinuity by using the SR technique of [6].

In the same fashion, we shall see that ENO reconstruction (also combined with SR) techniques in the hat-averaged multiresolution context lead to very efficient data compression algorithms for piecewise smooth signals with a finite number of

δ -singularities. The space of such functions is used in vortex methods for the numerical solution of fluid dynamics problems.

For the sake of completeness, in the remainder of this section we describe briefly the ENO interpolation technique and Harten's SR.

2.1. ENO interpolation. To make the presentation simpler, we consider a grid $X = \{x_i\}$ in $[0, 1]$ with uniform spacing $h = x_{i+1} - x_i$ (see [1, 13] for generalizations to nonuniform grids and also to higher dimensions).

Let $H(x) \in \mathcal{C}[0, 1]$. Using the notation of section 3, we call $\tilde{\mathcal{D}}H = (H_j)_j$, where $H_j = H(x_j)$. Let $\mathcal{I}(x; \tilde{\mathcal{D}}H)$ be any piecewise polynomial function that interpolates $H(x)$ on the grid X .

If the interpolatory technique is of order r , we have

$$\mathcal{I}(x; \tilde{\mathcal{D}}H) = q_j(x; \tilde{\mathcal{D}}H) \quad \text{for } x \in [x_{j-1}, x_j],$$

where $q_j(x; \tilde{\mathcal{D}}H)$ is a polynomial of degree $r - 1$ such that $q_j(x_{j-1}; \tilde{\mathcal{D}}H) = H_{j-1}$ and $q_j(x_j; \tilde{\mathcal{D}}H) = H_j$. The set of r grid points used to construct the polynomial piece $q_j(x; \tilde{\mathcal{D}}H)$ forms the *stencil* \mathcal{S}_j associated with the interval $[x_{j-1}, x_j]$. The grid points x_{j-1} and x_j must always belong to \mathcal{S}_j .

The essential feature of the ENO interpolatory technique is a stencil selection procedure that attempts to choose the stencil \mathcal{S}_j within a region of smoothness of $H(x)$.

For each interval $[x_{j-1}, x_j]$, we consider all possible stencils of $r \geq 2$ points that include x_{j-1} and x_j ,

$$\{x_{j-r+1}, \dots, x_j\}, \dots, \{x_{j-1}, \dots, x_{j+r-2}\}$$

and select the stencil for which $H(x)$ is "smoother" in some sense. We will do this by fixing $i(j)$, an index related to the initial point of the stencil. For notational purposes, we assume that $i(j)$ is the second point in the final stencil. Notice that if $r = 2$, $\mathcal{S}_j = \{x_{j-1}, x_j\}$ and no selection technique is needed. We assume then that $r > 2$.

In [12], the authors describe the following two stencil selection procedures.

ALGORITHM I. Hierarchical choice of stencil:

```

Choose  $i_0(j) = j$ 
if  $|H(x_{j-2}, x_{j-1}, x_j)| < |H(x_{j-1}, x_j, x_{j+1})|$ 
     $i_{1j} = i_0(j) - 1$ 
else
     $i_{1j} = i_0(j)$ 
endif
for  $l = 1, \dots, r - 3$ 
    if  $|H(x_{i_l(j)-2}, \dots, x_{i_l(j)+l})| < |H(x_{i_l(j)-1}, \dots, x_{i_l(j)+l+1})|$ 
         $i_{l+1}(j) = i_l(j) - 1$ 
    else
         $i_{l+1}(j) = i_l(j)$ 
    endif
end
 $i(j) = i_{r-2}(j).$ 

```

ALGORITHM II. Nonhierarchical choice of the stencil:

Choose $i(j)$ so that $ H(x_{i(j)-1}, \dots, x_{i(j)+r-2}) = \min\{ H(x_{l-1}, \dots, x_{l+r-2}) , \quad j-r+2 \leq l \leq j\}.$
--

Notice that if $j-r+2 \leq i(j) \leq j$, then $x_{j-1}, x_j \in \mathcal{S}_j$ in both cases.

The hierarchical choice of the stencil is the preferred one in most situations. Algorithm II chooses the stencil according to the monotonicity properties of $H^{(k)}$, and its performance in the preasymptotic range is, in general, poorer than that of Algorithm I. In our context, this becomes very important since we shall be using the ENO technique on various resolution levels, some of which may well be in the preasymptotic range.

Let us assume that $H(x)$ is a continuous, piecewise smooth function and that $H'(x)$ has discontinuity at $x_d \in [x_{j-1}, x_j]$ (we say then that $H(x)$ has a *corner* at x_d). When $[H']_{x_d} = H'(x_d+0) - H'(x_d-0) = O(1)$, an analysis of the stencil selection procedure (see, e.g., [4]) reveals that both Algorithms I and II lead to stencils such that

$$\mathcal{S}_{j-1} \cap \mathcal{S}_{j+1} = \emptyset.$$

In this case both stencil selection procedures lead to interpolatory polynomials that satisfy

$$H(x) = q_l(x; \tilde{\mathcal{D}}H) + O(h^r \|H^r\|), \quad x \in [x_{l-1}, x_l], \quad l \leq j-1, \quad l \geq j+1.$$

However, the smooth polynomial piece $q_j(x; \tilde{\mathcal{D}}H)$ can only be a first-order approximation to the function $H(x)$ at the $[x_{j-1}, x_j]$ cell, which contains the singularity.

On the other hand, interpolatory techniques based on a fixed choice of stencil lead to polynomial interpolants q_l that are only first-order approximations to $H(x)$ as soon as their stencil crosses x_d . The accuracy of the piecewise polynomial interpolant is thus degraded over a large region around the singularity (its range depends on the degree of the polynomial pieces, i.e., the number of points in the stencil).

It is proven in [4] that, if the only singularities of $H(x)$ are corners and they are well separated (it is possible to choose a stencil in the smooth part of the function), then the ENO interpolation procedure leads to a piecewise interpolant that satisfies

$$(2.2) \quad \frac{d^m}{dx^m} \mathcal{I}(x \pm 0; \tilde{\mathcal{D}}H) = \frac{d^m}{dx^m} H(x) + O(h^{r-m}), \quad 0 \leq m \leq r-1,$$

except when x belongs to an interval containing a corner. As a result, the accuracy of the ENO piecewise polynomial interpolant is maintained over the largest possible region.

If we know the location of the singularity within the cell (or a sufficiently good approximation to it), the definition of the piecewise interpolant $\mathcal{I}(x; \tilde{\mathcal{D}}H)$ can be modified to keep the relation

$$H(x) = \mathcal{I}(x; \tilde{\mathcal{D}}H) + O(h^r)$$

valid over an even larger region. This is the basic idea behind Harten's SR technique.

2.2. The subcell resolution technique. Let us assume that $H(x)$ is a continuous function with a corner at $x_d \in (x_{j-1}, x_j)$. Then, the ENO interpolants

$q_{j\pm 1}(x; \tilde{\mathcal{D}}H)$ satisfy

$$(2.3) \quad H(x) = q_{j-1}(x; \tilde{\mathcal{D}}H) + O(h^r), \quad x \in [x_{j-2}, x_{j-1}],$$

$$(2.4) \quad H(x) = q_{j+1}(x; \tilde{\mathcal{D}}H) + O(h^r), \quad x \in [x_j, x_{j+1}].$$

The location of the corner, x_d , can be recovered using the following function:

$$(2.5) \quad G_j(x) := q_{j+1}(x; \tilde{\mathcal{D}}H) - q_{j-1}(x; \tilde{\mathcal{D}}H).$$

Using Taylor expansions in regions of smoothness, it is not hard to prove that

$$G_j(x_{j-1}) \cdot G_j(x_j) = a \cdot (a-1) [H']_{x_d}^2 h^2 + O(h^3),$$

where $x_d = x_j - ah$, $0 < a < 1$.

Therefore, if h is sufficiently small, there is a root of G_j in (x_{j-1}, x_j) . Let $\theta_j \in (x_{j-1}, x_j)$ be such that $G_j(\theta_j) = 0$. We consider θ_j to be an approximation to x_d , but how good is this approximation? Let us consider the special case

$$(2.6) \quad H(x) = \begin{cases} P_L(x), & x \leq x_d, \\ P_R(x), & x \geq x_d, \end{cases} \quad \text{where} \quad \begin{cases} P_L(x_d) = P_R(x_d), & P'_L(x_d) \neq P'_R(x_d), \\ \max(\deg(P_L), \deg(P_R)) \leq r-1. \end{cases}$$

By construction, we must have

$$q_{j-1}(x; \tilde{\mathcal{D}}H) = P_L(x), \quad q_{j+1}(x; \tilde{\mathcal{D}}H) = P_R(x),$$

which implies that $\theta_j = x_d$. In the general case, it can be proven (see [6] or [4]) that

$$|\theta_j - x_d| = O(h^r).$$

Thus, using the ENO polynomial pieces at each side of the singularity, we can recover the location of an isolated discontinuity in the derivative of a continuous function, up to the order of the truncation error. This information can be used to modify the polynomial piece corresponding to the cell $[x_{j-1}, x_j]$ as follows: Instead of taking the polynomial $q_j(x; \tilde{\mathcal{D}}H)$ as the approximation of $H(x)$ in this interval, we extend the polynomial pieces at the left and right neighboring intervals up to the point θ_j , where they intersect. The new piecewise polynomial interpolant has the following form:

$$(2.7) \quad \mathcal{I}^{SR}(x; \tilde{\mathcal{D}}H) = \begin{cases} q_l(x; \tilde{\mathcal{D}}H), & x \in [x_{l-1}, x_l], \quad l \neq j, \\ q_{j-1}(x; \tilde{\mathcal{D}}H), & x \in [x_{j-1}, \theta_j], \\ q_{j+1}(x; \tilde{\mathcal{D}}H), & x \in [\theta_j, x_j]. \end{cases}$$

It is then clear that

$$\mathcal{I}^{SR}(x_l; \tilde{\mathcal{D}}H) = H(x_l), \quad x_l \in X,$$

and

$$\frac{d^m}{dx^m} \mathcal{I}^{SR}(x \pm 0; \tilde{\mathcal{D}}H) = \frac{d^m}{dx^m} H(x) + O(h^{r-m}), \quad 0 \leq m \leq r-1,$$

at all points except for an $O(h^r)$ band around x_d which is now the only region in which the accuracy is degraded (instead of the whole interval $[x_{j-1}, x_j]$). It follows that if $H(x)$ is as in (2.6), then $\mathcal{I}^{SR}(x; \tilde{D}H) = H(x)$, i.e., the modified reconstruction, is exact.

The basic principle underlying the SR technique is in fact very simple:

Use accurate reconstructions at the cells neighboring a singularity to recover the singularity within the cell.

It can be applied also to weaker singularities. Suppose that $H(x)$ has a discontinuity in its $(q+1)$ st derivative ($q < r$), i.e., $H(x) \in \mathcal{C}^q$ and $[H^{(q+1)}]_{x_d} = O(1)$, where $x_d \in [x_{j-1}, x_j]$. If the polynomial functions $q_{j-1}(x; \tilde{D}H)$ and $q_{j+1}(x; \tilde{D}H)$ are constructed using only data from the smooth part of $H(x)$, or in other words if $\mathcal{S}_{j-1} \cap \mathcal{S}_{j+1} = \emptyset$, then we have

$$\frac{d^m}{dx^m} q_{j-1}(x; \tilde{D}H) = \frac{d^m}{dx^m} H(x) + O(h^{r-m}), \quad x \in [x_{j-2}, x_{j-1}], \quad 0 \leq m \leq r-1,$$

$$\frac{d^m}{dx^m} q_{j+1}(x; \tilde{D}H) = \frac{d^m}{dx^m} H(x) + O(h^{r-m}), \quad x \in [x_j, x_{j+1}], \quad 0 \leq m \leq r-1.$$

Again using Taylor expansions, we can prove that

$$G_j^{(q)}(x_j) \cdot G_j^{(q)}(x_{j-1}) < 0.$$

Thus, there is a root of $G_j^{(q)}(x)$ in $[x_{j-1}, x_j]$. Furthermore, if the root is θ_j , it is not hard to prove (see [4]) that

$$|\theta_j - x_d| = O(h^{r-q}).$$

It follows that replacing $\mathcal{I}(x; \tilde{D}H)$ by $\mathcal{I}^{SR}(x; \tilde{D}H)$ in (2.7) with θ_j now being the root of $G_j^{(q)}(x)$ in $[x_{j-1}, x_j]$ leads to a reconstruction technique which is exact for the corresponding piecewise polynomial problem (2.6) with

$$P_L^{(m)}(x_d) = P_R^{(m)}(x_d), \quad 0 \leq m \leq q, \quad \text{and} \quad P_L^{(q+1)}(x_d) \neq P_R^{(q+1)}(x_d).$$

The key to the success of the SR technique is the accuracy of the polynomial pieces $q_{j\pm 1}$. The ENO technique ensures (2.3) and (2.4) when the singularity is a corner. However, when dealing with weaker singularities, Algorithm I might lead to a selection of stencil such that \mathcal{S}_{j-1} or \mathcal{S}_{j+1} (or both) cross the singularity. The phenomenon is analyzed in detail in [4] where it is observed that, to maintain the accuracy of the polynomial pieces, one needs to switch to Algorithm II in cells neighboring weak singularities.

In practice, we like to work with Algorithm I because of its better overall behavior in regions of smoothness. Thus one needs to identify those cells that are suspected of harboring a weak discontinuity and recompute the polynomial pieces at the neighboring cells.

We would like to finish this section with a remark: If $H(x)$ has a corner at a grid point, say x_j , then q_j and q_{j+1} are accurate representations of $H(x)$ within their respective intervals; however, if x_j is a weaker discontinuity, the results of [4] indicate that \mathcal{S}_j and/or \mathcal{S}_{j+1} might cross the singularity. This leads to a degradation of the accuracy of q_j and/or q_{j+1} . We address this issue in section 5.

3. Basic background on the hat-average multiresolution framework.

This section is a brief review of section 8 in [2]. Here we describe only those elements of the hat-average setting that we find necessary for the development of this paper. We refer the reader to [2] for more details and for proofs of all the facts we state below.

Let us consider the unit interval $[0, 1]$ and the sequence of nested dyadic grids $X^k = \{x_i^k\}_{i=0}^{J_k}$, $x_i^k = ih_k$, $h_k = 2^{-k}h_0$, $J_k = 2^k J_0$.

The discretization procedure is based on integrating against scaled translates of the hat function:

$$(3.1) \quad \omega(x) = \begin{cases} 1+x, & -1 \leq x \leq 0, \\ 1-x, & 0 \leq x \leq 1, \\ 0 & \text{otherwise,} \end{cases}$$

that is,

$$(3.2) \quad (\mathcal{D}_k f)_i = \bar{f}_i^k = \langle f, \omega_i^k \rangle, \quad \omega_i^k = \frac{1}{h_k} \omega\left(\frac{x}{h_k} - i\right).$$

Notice that it is sufficient to consider weighted averages \bar{f}_i^k for $1 \leq i \leq N_k = J_k - 1$ since these averages contain information on f over the whole interval $[0, 1]$. Moreover, since the hat function is continuous, a finite number of (isolated) δ -type singularities are allowed. Thus,

$$\mathcal{D}_k : \mathcal{F} \longrightarrow S^k,$$

where \mathcal{F} is the space of piecewise smooth functions in $[0, 1]$ with a finite number of δ -type singularities in $(0, 1)$, and S^k is the space of finite sequences of $N_k = J_k - 1$ components.

The hat function satisfies the following dilation relation:

$$(3.3) \quad \omega(x) = \frac{1}{2}[\omega(2x-1) + 2\omega(2x) + \omega(2x+1)].$$

This implies that

$$(3.4) \quad \bar{f}_i^{k-1} = \frac{1}{4}\bar{f}_{2i-1}^k + \frac{1}{2}\bar{f}_{2i}^k + \frac{1}{4}\bar{f}_{2i+1}^k.$$

Therefore the decimation matrix (an $N_{k-1} \times N_k$ matrix) is given explicitly by the following expression:

$$(3.5) \quad (D_k^{k-1})_{ij} = \frac{1}{4}\delta_{2i-1,j} + \frac{1}{2}\delta_{2i,j} + \frac{1}{4}\delta_{2i+1,j}.$$

Because of the dilation relation satisfied by the hat function, the prediction errors satisfy

$$(3.6) \quad e_{2i}^k = -\frac{1}{2}e_{2i-1}^k - \frac{1}{2}e_{2i+1}^k.$$

This leads to the following algorithmic description of the transfer operators G_k and E_k :

$$(3.7) \quad d^k = G_k e^k, \quad d_i^k = e_{2i-1}^k, \quad 1 \leq i \leq J_{k-1},$$

$$(3.8) \quad e^k = E_k d^k, \quad \begin{cases} e_{2i-1}^k &= d_i^k, & 1 \leq i \leq J_{k-1}, \\ e_{2i}^k &= -\frac{1}{2}(d_i^k + d_{i+1}^k), & 1 \leq i \leq J_{k-1} - 1. \end{cases}$$

To complete the construction of a multiresolution scheme, we need a working definition of the prediction operators. This is accomplished by the *reconstruction via second primitive technique*. A brief description of the technique is as follows:

Let $f = f_p + \sum_l h_l \delta(x - a_l)$, $0 < a_l < 1$, be represented as the sum of a piecewise smooth function in $[0, 1]$, f_p , with a finite number of δ -jumps in $(0, 1)$. Define its “second primitive” as

$$(3.9) \quad H(x) = \int_0^x \int_0^y f_p(z) dz dy + \sum h_l (x - a_l)_+ - qx,$$

where

$$(x - a)_+ = \begin{cases} x - a & \text{if } x > a, \\ 0 & \text{otherwise} \end{cases} \quad \text{and} \quad q = \int_0^1 \int_0^y f_p(z) dz dy + \sum h_l.$$

Then $H(x)$ is a continuous piecewise smooth function which satisfies the following relation:

$$(3.10) \quad \bar{f}_i^k = \langle f, \omega_i^k \rangle = \frac{1}{h_k^2} (H_{i+1}^k - 2H_i^k + H_{i-1}^k), \quad 1 \leq i \leq J_k - 1,$$

where $H_i^k = H(x_i^k)$.

Relation (3.10) establishes a one-to-one correspondence between the sets $\{\bar{f}_i^k\}_{i=1}^{J_k-1}$ and $\{H_i^k\}_{i=1}^{J_k-1}$. Thus, knowledge of the hat-averages of a given function $f \in \mathcal{F}$ is equivalent to knowledge of the point values of its second primitive (3.9). We can then interpolate the point values of the “second primitive” by any interpolation procedure $\mathcal{I}_k(x; H^k)$ and define

$$(3.11) \quad (\mathcal{R}_k \bar{f}^k)(x) := \frac{d^2}{dx^2} \mathcal{I}_k(x; H^k).$$

On many occasions the interpolatory function is defined as

$$(3.12) \quad \mathcal{I}_k(x; H^k) = q_j^k(x; H^k) \quad \text{for } x \in [x_{j-1}^k, x_j^k],$$

where $q_j^k(x; H^k)$ is a smooth function, usually a polynomial. Its first derivative will then be a piecewise smooth function possibly with discontinuities at the grid points of the k th level; thus, its second derivative must be considered in the distribution sense. In fact, we shall have

$$(3.13) \quad (\mathcal{R}_k \bar{f}^k)(x) = \tilde{\mathcal{I}}_k(x) + \sum_{j=1}^{J_k-1} s_j^k \delta(x - x_j^k),$$

where $\tilde{\mathcal{I}}_k$ is defined as

$$(3.14) \quad \tilde{\mathcal{I}}_k(x) = \frac{d^2}{dx^2} q_j^k(x; H^k) \quad \text{for } x \in [x_{j-1}^k, x_j^k],$$

and

$$(3.15) \quad \begin{aligned} s_j^k &= \left[\frac{d}{dx} q_{j+1}^k(x; H^k) - \frac{d}{dx} q_j^k(x; H^k) \right]_{x=x_j^k} \\ &= \mathcal{I}_k'(x_j^k + 0; H^k) - \mathcal{I}_k'(x_j^k - 0; H^k). \end{aligned}$$

We proved in Part I [2] that \mathcal{R}_k in (3.13) is a proper reconstruction procedure in the hat-weighted multiresolution setting, that is, it satisfies $\mathcal{D}_k \mathcal{R}_k = I_k$. Moreover, if the order of the interpolation is r , then the order of \mathcal{R}_k in (3.11) is $p = r - 2$. The prediction operator is now computed from \mathcal{R}_k using (1.7), and this leads [2] to

$$(3.16) \quad \begin{aligned} (P_{k-1}^k \bar{f}^{k-1})_j &= \frac{1}{h_k^2} (\mathcal{I}_{k-1}(x_{j-1}^k; H^{k-1}) - 2\mathcal{I}_{k-1}(x_j^k; H^{k-1}) \\ &\quad + \mathcal{I}_{k-1}(x_{j+1}^k; H^{k-1})). \end{aligned}$$

Once all the necessary ingredients of the multiresolution scheme have been specified, we can give an explicit description of the hat-based multiresolution transform and its inverse,

$$\bar{f}^L \rightarrow M \bar{f}^L \text{ (Encoding)}$$

$$(3.17) \quad \begin{array}{l} \textbf{for } k = L, \dots, 1 \\ \quad \textbf{for } i = 1, \dots, J_{k-1} - 1 \\ \quad \quad \bar{f}_i^{k-1} = \frac{1}{4}(\bar{f}_{2i-1}^k + 2\bar{f}_{2i}^k + \bar{f}_{2i+1}^k) \\ \quad \textbf{end} \\ \quad \textbf{for } i = 1, \dots, J_{k-1} \\ \quad \quad d_i^k = \bar{f}_{2i-1}^k - (P_{k-1}^k \bar{f}^{k-1})_{2i-1} \\ \quad \textbf{end} \\ \textbf{end} \\ M \bar{f}^L = \{\bar{f}^0, d^1, \dots, d^L\} \end{array}$$

$$M \bar{f}^L \rightarrow M^{-1} M \bar{f}^L \text{ (Decoding)}$$

$$(3.18) \quad \begin{array}{l} \textbf{for } k = 1, \dots, L \\ \quad \textbf{for } i = 1, \dots, J_{k-1} \\ \quad \quad \bar{f}_{2i-1}^k = (P_{k-1}^k \bar{f}^{k-1})_{2i-1} + d_i^k \\ \quad \textbf{end} \\ \quad \textbf{for } i = 1, \dots, J_{k-1} - 1 \\ \quad \quad \bar{f}_{2i}^k = 2\bar{f}_i^{k-1} - \frac{1}{2}(\bar{f}_{2i-1}^k + \bar{f}_{2i+1}^k) \\ \quad \textbf{end} \\ \textbf{end} \end{array}$$

In algorithms (3.17) and (3.18), only the predicted values at the odd-indexed grid points are computed. With the definition given in (3.12), relation (3.16) becomes (see Figure 3.1)

$$(P_{k-1}^k \bar{f}^{k-1})_{2i-1} = \frac{1}{h_k^2} [q_i^{k-1}(x_{2i-2}^k) - 2q_i^{k-1}(x_{2i-1}^k) + q_i^{k-1}(x_{2i}^k)].$$

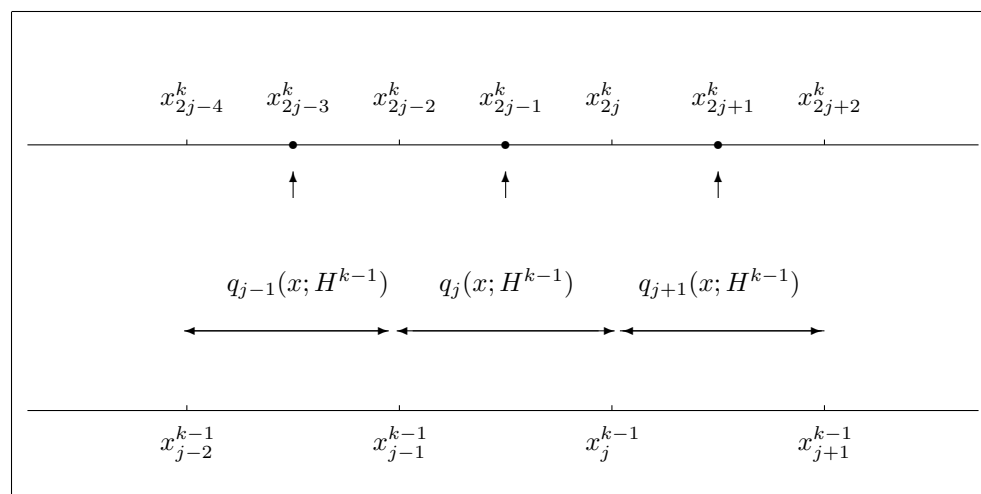


FIG. 3.1. The polynomial pieces.

Using the Newton form of the polynomial piece $q_l^{k-1}(x)$ and Remark 3.1, it is easy to write $(P_{k-1}^k \bar{f}^{k-1})_{2i-1}$ in terms of $\{\bar{f}_i^{k-1}\}$ and their divided differences.

Remark 3.1. Because of (3.10), the divided differences table constructed with the sampled values at a given resolution level $\{\bar{f}^k\}$ can be related to the table of divided differences of $H(x)$ on that resolution level. In fact, with the usual notation,

$$\begin{cases} \bar{f}[x_j^k, x_{j+1}^k] &= \frac{1}{h_k} (\bar{f}_{j+1}^k - \bar{f}_j^k), \\ \bar{f}[x_j^k, \dots, x_{j+n}^k] &= \frac{1}{nh_k} (\bar{f}[x_{j+1}^k, \dots, x_{j+n}^k] - \bar{f}[x_j^k, \dots, x_{j+n-1}^k]), \quad n > 1, \end{cases}$$

$$\begin{cases} H[x_j^k, x_{j+1}^k] &= \frac{1}{h_k} (H_{j+1} - H_j), \\ H[x_j^k, \dots, x_{j+n}^k] &= \frac{1}{nh_k} (H[x_{j+1}^k, \dots, x_{j+n}^k] - H[x_j^k, \dots, x_{j+n-1}^k]), \quad n > 1, \end{cases}$$

it is easy to prove that

$$(3.19) \quad \bar{f}[x_j^k, \dots, x_{j+n}^k] = (n+1)(n+2)H[x_{j-1}^k, \dots, x_{j+n+1}^k].$$

Thus, second- and higher-order divided differences of $H(x)$ on each grid X^k can be expressed in terms of $(\mathcal{D}f)$ and its divided differences. Hence, the role of $H(x)$ is that of a design tool, and it never needs to be computed explicitly.

The description of the prediction operator in terms of the reconstruction via “second primitive” links the hat-average and the interpolatory multiresolution settings considered in [7, 8, 9]. The interpolation technique used to define \mathcal{R}_k in (3.11) also provides a reconstruction operator for an interpolatory setting. Thus, the application of a hat-average multiresolution scheme to a function $f \in \mathcal{F}$ is intimately connected to the application of a specific interpolatory multiresolution scheme to its second primitive. Both settings play a role in our later development; thus, to distinguish between the two of them we have reserved the symbols \mathcal{D}_k , \mathcal{R}_k , D_k^{k-1} , and P_{k-1}^k for the hat-average multiresolution setting and the symbols $\tilde{\mathcal{D}}_k$, $\tilde{\mathcal{R}}_k$, \tilde{D}_k^{k-1} , \tilde{P}_{k-1}^k for the

interpolatory setting, i.e., given a function $H(x) \in \mathcal{C}[0, 1]$, we have

$$\begin{aligned}
 (\tilde{\mathcal{D}}_k H)_i &= H_i^k = H(x_i^k), & 0 \leq i \leq J_k, \\
 \tilde{\mathcal{R}}_k H^k(x) &= \mathcal{I}_k(x; H^k) \equiv \mathcal{I}_k(x; \tilde{\mathcal{D}}_k H), & x \in [0, 1], \\
 (\tilde{\mathcal{D}}_k^{k-1} H^k)_i &= H_{2i}^{k-1} = H_i^{k-1}, & 0 \leq i \leq J_{k-1}, \\
 (\tilde{\mathcal{P}}_{k-1}^k H^{k-1})_i &= \mathcal{I}_{k-1}(x_i^k; H^{k-1}), & 0 \leq i \leq J_k.
 \end{aligned}
 \tag{3.20}$$

4. ENO reconstruction with SR in the hat-average context. The *reconstruction via second primitive* technique can be carried out using *any* interpolatory procedure. When the function to be interpolated, that is, $H(x)$, is smooth, it really makes no difference which interpolatory technique one decides to use. However, when $H(x)$ is only piecewise smooth, adaptive nonlinear interpolatory techniques such as the ENO interpolation maintain the full accuracy of the approximation over a much larger region than linear techniques of the same order. Thus ENO-based reconstruction operators have better compression capabilities than their linear counterparts.

Remark 4.1. Because of Remark 3.1, the stencil selection process, which is the heart of the ENO interpolation technique, can be carried out without explicit knowledge of $\tilde{\mathcal{D}}H$.

The region where the piecewise polynomial interpolant attains its full accuracy can be maximized using Harten's SR technique. In this section, we show that the ENO-SR interpolatory technique leads to a proper reconstruction procedure within the hat-average framework (i.e., (1.5) is satisfied). In addition we shall provide a working description of the prediction operator.

To fix ideas, we consider a grid $X = \{x_i\}$ in $[0, 1]$ with uniform spacing $h = x_{i+1} - x_i$ and assume that

$$f(x) = P(x) + \alpha \delta(x - x_d),$$

where $P(x)$ is smooth and $x_d \in (x_{j-1}, x_j)$. Its second primitive (3.9) has the following form:

$$H(x) = Q(x) + \alpha(x - x_d)_+ - qx,$$

where $Q(x)$ is a smooth function such that $Q'' = P$. Hence, $H(x)$ has a corner at x_d ($[H']_{x_d} = \alpha$) and is smooth otherwise. An ENO interpolation of $H(x)$ of order r leads to a piecewise polynomial function $\mathcal{I}(x; \tilde{\mathcal{D}}H)$ satisfying (2.2) except at the interval containing x_d . Notice that

$$s_l = \mathcal{I}'(x_l + 0; \tilde{\mathcal{D}}H) - \mathcal{I}'(x_l - 0; \tilde{\mathcal{D}}H) = O(h^{r-1}), \quad l \neq j - 1, j.$$

The SR technique substitutes the ENO piecewise polynomial interpolant, $\mathcal{I}(x; \tilde{\mathcal{D}}H)$, by $\mathcal{I}^{SR}(x; \tilde{\mathcal{D}}H)$ as defined in (2.7). Notice that $\mathcal{I}(x; \tilde{\mathcal{D}}H)$ and $\mathcal{I}^{SR}(x; \tilde{\mathcal{D}}H)$ are equivalent except at the cell containing the singularity, i.e., the modification is *local*. Using Lemma 5.1 in [2] and our observations in section 2, we can easily derive the ENO-SR reconstruction operator in the hat-average context:

$$\begin{aligned}
 (4.1) \quad \mathcal{R}^{SR}(x; \mathcal{D}f) &= \frac{d^2}{dx^2} \mathcal{I}^{SR}(x; \tilde{\mathcal{D}}H) \\
 &= \tilde{\mathcal{I}}^{SR}(x; \tilde{\mathcal{D}}H) + \hat{s}_j \delta(x - \theta_j) + \sum_{m \neq j-1, j} s_m \delta(x - x_m),
 \end{aligned}$$

where

$$(4.2) \quad \theta_j \in (x_{j-1}, x_j), \quad G_j(\theta_j) = 0, \quad G_j(x) = q_{j+1}(x; \tilde{\mathcal{D}}H) - q_{j-1}(x; \tilde{\mathcal{D}}H),$$

$$(4.3) \quad \tilde{\mathcal{I}}^{SR}(x; \tilde{\mathcal{D}}H) = \begin{cases} \frac{d^2}{dx^2} q_l(x; \tilde{\mathcal{D}}H), & x \in [x_{l-1}, x_l], \quad l \neq j, \\ \frac{d^2}{dx^2} q_{j-1}(x; \tilde{\mathcal{D}}H), & x \in [x_{j-1}, \theta_j], \\ \frac{d^2}{dx^2} q_{j+1}(x; \tilde{\mathcal{D}}H), & x \in [\theta_j, x_j], \end{cases}$$

and

$$s_l = \left[\frac{d}{dx} q_{l+1}(x; \tilde{\mathcal{D}}H) - \frac{d}{dx} q_l(x; \tilde{\mathcal{D}}H) \right]_{x=x_l}, \quad l \neq j-1, j,$$

$$\hat{s}_j = \left[\frac{d}{dx} q_{j+1}(x; \tilde{\mathcal{D}}H) - \frac{d}{dx} q_{j-1}(x; \tilde{\mathcal{D}}H) \right]_{x=\theta_j}.$$

Let us prove that $\mathcal{R}^{SR}(x; \mathcal{D}f)$ satisfies $\mathcal{D}\mathcal{R}^{SR} = I$. Observe that

$$\begin{aligned} \langle \mathcal{R}^{SR}(x; \mathcal{D}f), \omega_l \rangle &= \langle \tilde{\mathcal{I}}^{SR}(x; \tilde{\mathcal{D}}H), \omega_l \rangle + \hat{s}_j \langle \delta(x - \theta_j), \omega_l \rangle \\ &\quad + \sum_{m \neq j, j-1} s_m \langle \delta(x - x_m), \omega_l \rangle. \end{aligned}$$

Because of the *local* character of the SR technique, $\mathcal{R}^{SR}(x; \mathcal{D}f)$ coincides with $\mathcal{R}(x; \mathcal{D}f)$ (the reconstruction obtained by differentiating the ENO interpolant $\mathcal{I}(x; \tilde{\mathcal{D}}H)$) except at the cell containing the singularity. Thus, we have

$$(4.4) \quad \begin{aligned} (\mathcal{D}\mathcal{R}^{SR}(x; \mathcal{D}f))_l &= \langle \mathcal{R}^{SR}(x; \mathcal{D}f), \omega_l \rangle \\ &= \langle \mathcal{R}(x; \mathcal{D}f), \omega_l \rangle = (\mathcal{D}f)_l, \quad l \neq j-1, j. \end{aligned}$$

On the other hand, integration by parts (see [2, Lemma 8.2]) shows that

$$\begin{aligned} (\mathcal{D}\mathcal{R}^{SR}(x; \mathcal{D}f))_j &= \langle \tilde{\mathcal{I}}^{SR}(x; \tilde{\mathcal{D}}H), \omega_j \rangle + \hat{s}_j \langle \delta(x - \theta_j), \omega_j \rangle \\ &= -\hat{s}_j \omega_j(\theta_j) + \frac{1}{h^2} [H(x_{j+1}) - 2H(x_j) + H(x_{j-1})] \\ &\quad + \frac{1}{h^2} [q_{j+1}(\theta_j, \tilde{\mathcal{D}}H) - q_{j-1}(\theta_j, \tilde{\mathcal{D}}H)] + \hat{s}_j \omega_j(\theta_j), \end{aligned}$$

i.e.,

$$(4.5) \quad (\mathcal{D}\mathcal{R}^{SR}(x; \mathcal{D}f))_j = (\mathcal{D}f)_j + \frac{1}{h^2} G_j(\theta_j) = (\mathcal{D}f)_j.$$

In the same fashion, it is easy to see that

$$(4.6) \quad (\mathcal{D}\mathcal{R}^{SR}(x; \mathcal{D}f))_{j-1} = (\mathcal{D}f)_{j-1} - \frac{1}{h^2} G_j(\theta_j) = (\mathcal{D}f)_{j-1}.$$

Relations (4.4), (4.5), and (4.6) prove our claim. Moreover, our analysis in section 2.2 shows that $\mathcal{R}^{SR}(x; \mathcal{D}f)$ is exact when $P(x)$ is a polynomial function such that $\deg(P) \leq p-1 = r-3$.

To use the ENO-SR reconstruction technique as our approximation tool in the hat-average multiresolution setting, we need a working description of the corresponding prediction operator $(P^{SR})_{k-1}^k = \mathcal{D}_k \mathcal{R}_{k-1}^{SR}$.

Let us consider the sequence of nested dyadic grids X^k of section 3 and assume that $x_d \in (x_{j-1}^{k-1}, x_j^{k-1})$. We then have

$$\begin{aligned} \mathcal{R}_{k-1}^{SR}(x; \bar{f}^{k-1}) &= \frac{d^2}{dx^2} \mathcal{I}_{k-1}^{SR}(x; H^{k-1}) \\ &= \tilde{\mathcal{I}}_{k-1}^{SR}(x; H^{k-1}) + \hat{s}_j^{k-1} \delta(x - \theta_j^{k-1}) + \sum_{\substack{m=1 \\ m \neq j-1, j}}^{J_{k-1}-1} s_m^{k-1} \delta(x - x_m^{k-1}), \end{aligned}$$

where

$$\theta_j^{k-1} \in (x_{j-1}^{k-1}, x_j^{k-1}), \quad G_j^{k-1}(\theta_j^{k-1}) = 0, \quad G_j^{k-1}(x) = q_{j+1}^{k-1}(x; H^{k-1}) - q_{j-1}^{k-1}(x; H^{k-1}),$$

$$\tilde{\mathcal{I}}_{k-1}^{SR}(x; H^{k-1}) = \begin{cases} \frac{d^2}{dx^2} q_l^{k-1}(x; H^{k-1}), & x \in [x_{l-1}^{k-1}, x_l^{k-1}], \quad l \neq j, \\ \frac{d^2}{dx^2} q_{j-1}^{k-1}(x; H^{k-1}), & x \in [x_{j-1}^{k-1}, \theta_j^{k-1}], \\ \frac{d^2}{dx^2} q_{j+1}^{k-1}(x; H^{k-1}), & x \in [\theta_j^{k-1}, x_j^{k-1}], \end{cases}$$

and

$$\begin{aligned} s_l^{k-1} &= \left[\frac{d}{dx} q_{l+1}^{k-1}(x; H^{k-1}) - \frac{d}{dx} q_l^{k-1}(x; H^{k-1}) \right]_{x_l^{k-1}}, \quad l \neq j-1, j, \\ \hat{s}_j^{k-1} &= \left[\frac{d}{dx} q_{j+1}^{k-1}(x; H^{k-1}) - \frac{d}{dx} q_{j-1}^{k-1}(x; H^{k-1}) \right]_{x=\theta_j^{k-1}}. \end{aligned}$$

Hence,

$$\begin{aligned} (4.7) \quad ((P^{SR})_{k-1}^k \bar{f}^{k-1})_l &= \langle \mathcal{R}_{k-1}^{SR}(x; \bar{f}^{k-1}), \omega_l^k \rangle \\ &= \langle \tilde{\mathcal{I}}_{k-1}^{SR}(x; H^{k-1}), \omega_l^k \rangle + \hat{s}_j^{k-1} \omega_l^k(\theta_j^{k-1}) \\ &\quad + \sum_{\substack{m=1 \\ m \neq j-1, j}}^{J_{k-1}-1} s_m^{k-1} \omega_l^k(x_m^{k-1}). \end{aligned}$$

Since $\text{supp}(\omega_l^k) = [x_{l-1}^k, x_{l+1}^k]$, the local character of the SR technique implies

$$\langle \mathcal{R}_{k-1}^{SR}(x; \bar{f}^{k-1}), \omega_l^k \rangle = \langle \mathcal{R}_{k-1}(x; \bar{f}^{k-1}), \omega_l^k \rangle, \quad l \neq 2j-2, 2j-1, 2j,$$

or, in other words,

$$((P^{SR})_{k-1}^k \bar{f}^{k-1})_l = (P_{k-1}^k \bar{f}^{k-1})_l, \quad l \neq 2j-2, 2j-1, 2j.$$

The SR technique modifies only the polynomial piece at the cell that contains a singularity. An immediate consequence of this fact is that the prediction operator does not change outside of the area where the δ -singularity affects the sampled data.

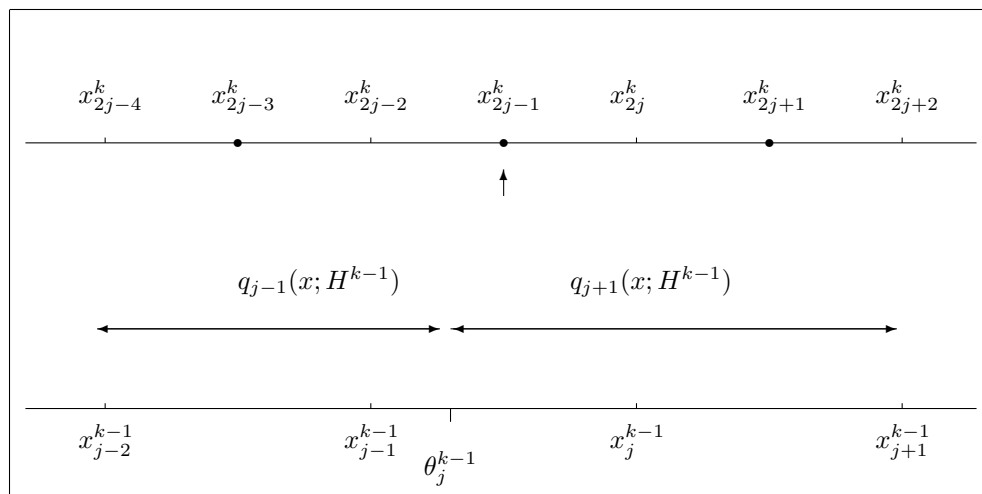


FIG. 4.1. The polynomial pieces in SR.

The computation of the predicted value at the middle point of the singular cell can be carried out from (4.7) by integration by parts. A typical situation is depicted in Figure 4.1. In the case displayed in the figure, we obtain

$$\theta_j^{k-1} \in [x_{2j-2}^k, x_{2j-1}^k],$$

$$((P^{SR})_{k-1}^k \bar{f}^{k-1})_{2j-1} = \frac{1}{h_k^2} [q_{j+1}^{k-1}(x_{2j}^k) - 2q_{j+1}^{k-1}(x_{2j-1}^k) + q_{j-1}^{k-1}(x_{2j-2}^k)].$$

Also,

$$\theta_j^{k-1} \in [x_{2j-1}^k, x_{2j}^k],$$

$$((P^{SR})_{k-1}^k \bar{f}^{k-1})_{2j-1} = \frac{1}{h_k^2} [q_{j+1}^{k-1}(x_{2j}^k) - 2q_{j-1}^{k-1}(x_{2j-1}^k) + q_{j-1}^{k-1}(x_{2j-2}^k)].$$

Even though we do not have the same polynomial piece on the right-hand side of these expressions, it is not difficult to write either of them in terms of $\{\bar{f}_i^{k-1}\}$ and their divided differences. We assume that $\mathcal{S}_{j-1} \cap \mathcal{S}_{j+1} = \emptyset$; this should be the case if each stencil belongs to the smooth part of the function. Then

$$(4.8) \quad q_{j-1}^{k-1}(x) = H(x_{j-1}^{k-1}) + H[x_{j-1}^{k-1}, x_{j-2}^{k-1}](x - x_{j-1}^{k-1}) \\ + \cdots + \sum_{m=3}^r H[x_{j-1}^{k-1}, \dots, x_{j-m}^{k-1}](x - x_{j-1}^{k-1}) \cdots (x - x_{j-m+1}^{k-1}),$$

$$(4.9) \quad q_{j+1}^{k-1}(x) = H(x_j^{k-1}) + H[x_j^{k-1}, x_{j+1}^{k-1}](x - x_j^{k-1}) \\ + \cdots + \sum_{m=2}^{r-1} H[x_j^{k-1}, \dots, x_{j+m}^{k-1}](x - x_j^{k-1}) \cdots (x - x_{j+m-1}^{k-1}).$$

It is not too difficult to prove, using Remark 3.1, that if $\theta_j^{k-1} \in [x_{2j-1}^k, x_{2j}^k]$, then

$$\begin{aligned} & ((P^{SR})_{k-1}^k \bar{f}^{k-1})_{2j-1} \\ &= 4\bar{f}_{j-1}^{k-1} - \frac{2}{h_k^2} \sum_{m=3}^{p+2} \frac{\bar{f}[x_{j-2}^{k-1}, \dots, x_{j-m+1}^{k-1}]}{(m-1)(m-2)} (x_{2j-1}^k - x_{j-1}^{k-1}) \cdots (x_{2j-1}^k - x_{j-m+1}^{k-1}). \end{aligned}$$

An analogous expression, including only the sampled data at the $(k-1)$ st level, can be found when $\theta_j^{k-1} \in [x_{2j-2}^k, x_{2j-1}^k]$.

The ENO-SR strategy for $O(1)$ δ -singularities is as follows:

1. Sweep through the computational domain and compute the ENO reconstruction at each cell using Algorithm I.
2. Use the criterion $\mathcal{S}_{j-1} \cap \mathcal{S}_{j+1} = \emptyset$ to single out cells suspected of harboring singularities. We label each cell in which $\mathcal{S}_{j-1} \cap \mathcal{S}_{j+1} \neq \emptyset$ as “singular.”
3. Locate the discontinuity within the “singular” cell using the G -function.
4. At each “singular” cell, modify the ENO reconstruction via SR; that is, extend the reconstructions to the left and to the right of the “singular” cell up to the computed location of the singularity.

We do emphasize that the strategy is only a design tool. In practice, once a cell, say $[x_{j-1}^{k-1}, x_j^k]$, has been labeled as *singular* at a given resolution level, in this case level $k-1$, we need only to compute in a special manner $((P^{SR})_{k-1}^k \bar{f}^{k-1})_l$ for $l = 2j-2, 2j-1, 2j$. In order to do this, it is *not necessary* to know the explicit location of the approximate singularity θ_j^{k-1} , only its relative location with respect to the grid point x_{2j-1}^k , which can be found simply by checking the sign of

$$G_j^{k-1}(x_{2j-2}^k) \cdot G_j^{k-1}(x_{2j-1}^k).$$

The function $G_j^{k-1}(x) = q_{j+1}^{k-1}(x) - q_{j-1}^{k-1}(x)$ can also be expressed directly in terms of the samples \bar{f}^{k-1} , thus there is no need (once again) to use any explicit information on the second primitive $H(x)$.

To express $G_j^{k-1}(x)$ in terms of the values \bar{f}^{k-1} and their divided differences, we use Remark 3.1 for second- and higher-order terms and rewrite the zero- and first-order terms (LOT) as follows (use expressions (4.8) and (4.9) for $q_{j+1}^{k-1}(x)$ and $q_{j-1}^{k-1}(x)$, and drop the superindex notation):

$$\begin{aligned} LOT &= H(x_j) + H[x_j, x_{j+1}](x - x_j) - H(x_{j-1}) - H[x_{j-2}, x_{j-1}](x - x_{j-1}) \\ &= 2h^2 H[x_{j-2}, x_{j-1}, x_j] + (x - x_j) 2h \{H[x_{j-2}, x_{j-1}, x_j] + H[x_{j-1}, x_j, x_{j+1}]\} \\ &= h^2 \bar{f}_{j-1} + (x - x_j) h \{\bar{f}_{j-1} + \bar{f}_j\}. \end{aligned}$$

5. SR at “weaker” singularities. The SR technique can also be applied to correct the reconstruction in cells that contain *weaker* singularities, for example, jumps or corners in $f(x)$ which correspond to discontinuities in H'' and H''' , and also what we call *weak* δ -singularities, that is, δ -type singularities where $\alpha = O(h_L)$, where L is the highest resolution level employed. We shall refer to these as “small δ .” However, one needs to be careful when applying the SR technique to these *weak* singularities.

We observed in sections 2 and 4 that, if $f(x) = g(x) + \alpha\delta(x - x_d)$, with $x_d \in (x_{j-1}, x_j)$, $g(x)$ smooth, and $\alpha = O(1)$, we can use the fact that $\mathcal{S}_{j-1} \cap \mathcal{S}_{j+1} = \emptyset$ to mark out those intervals suspected of containing a δ -type singularity.

In [4] Donat carries out a detailed analysis of the preferred form of the ENO interpolation process, the hierarchical form. This analysis reveals that Algorithm I leads to a stencil selection such that $\mathcal{S}_{j-1} \cap \mathcal{S}_{j+1} = \emptyset$, when applied to a function $H(x)$ which is continuous and has an $O(1)$ discontinuity in H' (in our framework, this would correspond to an $O(1)$ δ -singularity in $f(x)$). If this is the case, the interpolating polynomials next to the cell containing the singularity maintain their full accuracy because they are constructed with data coming from smooth portions of the function; thus, the SR technique has all the correct ingredients to succeed.

However, the analysis in [4] reveals that Algorithm I might be fooled by a weaker discontinuity, for example, a discontinuity in H'' , which in our framework would be obtained if $f(x)$ has a jump. In this case the interpolating polynomials next to the singularity may be constructed from a stencil that crosses the singularity. The accuracy of such polynomial pieces is thus degraded, and the SR technique has no chance to succeed. The same happens with the other *weak* singularities.

In dealing with *weak* singularities, it becomes very important to isolate cells that are *suspected* of harboring a singularity. Once they are identified, the SR technique can be applied, provided we use accurate representations of the polynomial pieces to the left and to the right of the “singular” cell. This can be done by switching to Algorithm II at those cells (see [4]).

Then, the strategy of the ENO-SR in the case of *weaker* singularities is as follows:

1. Sweep through the computational domain and calculate the ENO reconstruction at each cell using Algorithm I.
2. The criterion $\mathcal{S}_{j-1} \cap \mathcal{S}_{j+1} = \emptyset$ indicates a possible discontinuity in $H'(x)$ of order $O(1)$ within the j th cell but cannot be used to detect *weaker* discontinuities. A more complete mechanism for the detection of singular cells is outlined below and completely specified in the appendix.
3. Decide if the *suspicious* cell contains a singularity by using the G -function of the cell. If the check is positive, we label the cell as “singular.”
4. If needed, recompute the reconstructions at cells neighboring a “singular” cell to ensure that the stencil is chosen from the smooth part of the function. In other words, stencils corresponding to cells close to a “singular” cell should not *cross* that cell.
5. At each “singular” cell, modify the ENO reconstruction via SR, that is, extend the reconstructions to the left and to the right of the “singular” cell up to the computed location of the singularity.

These five steps, as in the previous section, are to be applied at the interpolation level, i.e., they should be applied to the second primitive in the hat-average setting, and to the first primitive in the cell-average multiresolution setting. In practice, however, the strategy again becomes a design tool, and it can be carried out (as it should be) without explicit knowledge of the point values of $H(x)$. All that is required in the multiresolution schemes are the sampled values of the signal $f(x)$, that is, $\mathcal{D}f$.

When the singularity falls on a grid point, the basic ENO reconstruction procedure is not modified. If $x_d = x_j$ is a δ -singularity with $O(1)$ strength, then $\mathcal{S}_{j-1} \cap \mathcal{S}_j = \{x_j\}$ and all polynomial pieces have the desired accuracy. However, if $x_d = x_j$ is a *weak* singularity, Algorithm I might lead to singularity-crossing stencils at the neighboring cells. To maintain the highest possible accuracy, weak singularities at grid points also need to be identified. The polynomial pieces next to a *weak* singularity lying at a grid point should be recomputed using stencils that stay on a smooth side of the function.

To design a technique which will detect any of the aforementioned singularities,

TABLE 5.1
Divided differences of order 4.

Case $x_d \in (x_{j-1}, x_j)$, $x_d \not\approx x_j$, $x_d \not\approx x_{j-1}$				Case $x_d = x_j$			
	delta	jump	corner		delta	jump	corner
$dci4(j)$	$O(h_L/h^3)$	$O(1/h^2)$	$O(1/h)$	$dci4(j-1)$	$O(1)$	$O(1)$	$O(1)$
$dni4(j)$	$O(1)$	$O(1)$	$O(1)$	$dni4(j-1)$	$O(1)$	$O(1)$	$O(1)$
$dce4(j)$	$O(h_L/h^3)$	$O(1/h^2)$	$O(1/h)$	$dce4(j-1)$	$O(h_L/h^3)$	$O(1/h^2)$	$O(1/h)$
$dne4(j)$	$O(h_L/h^3)$	$O(1/h^2)$	$O(1/h)$	$dne4(j-1)$	$O(1)$	$O(1)$	$O(1)$
Case $x_d \approx x_j^-$				Case $x_d \approx x_{j-1}^+$			
	delta	jump	corner		delta	jump	corner
$dci4(j)$	$O(1)$	$O(1)$	$O(1)$	$dci4(j-1)$	$O(1)$	$O(1)$	$O(1)$
$dni4(j)$	$O(1)$	$O(1)$	$O(1)$	$dni4(j-1)$	$O(1)$	$O(1)$	$O(1)$
$dce4(j)$	$O(h_L/h^3)$	$O(1/h^2)$	$O(1/h)$	$dce4(j-1)$	$O(h_L/h^3)$	$O(1/h^2)$	$O(1/h)$
$dne4(j)$	$O(1)$	$O(1)$	$O(1)$	$dne4(j-1)$	$O(1)$	$O(1)$	$O(1)$

we had to consider at least the fourth-order divided differences of $H(x)$. To make the notation easier we define

$$H[j; n] := H[x_j, x_{j+1}, \dots, x_{j+n}].$$

Suppose we have a singularity at $x_d \in [x_{j-1}, x_j]$, say $x_d = x_j - ah$, $0 \leq a \leq 1$. Then the fourth-order divided differences satisfy

$$\begin{aligned} H[j; 4] &= O(1), \\ H[j-1; 4] &= \frac{1-a}{24h^3} [H']_d - \frac{(a-1)^2}{48h^2} [H'']_d - \frac{(a-1)^3}{144h} [H''']_d + O(1), \\ H[j-2; 4] &= \frac{(3a-2)}{24h^3} [H']_d + \frac{3a^2-4a}{48h^2} [H'']_d + \frac{4-6a^2+3a^3}{144h} [H''']_d + O(1), \\ H[j-3; 4] &= \frac{(1-3a)}{24h^3} [H']_d + \frac{1+2a-3a^2}{48h^2} [H'']_d + \frac{1+3a+3a^2-3a^3}{144h} [H''']_d + O(1), \\ H[j-4; 4] &= \frac{a}{24h^3} [H']_d + \frac{a^2}{48h^2} [H'']_d + \frac{a^3}{144h} [H''']_d + O(1), \\ H[j-5; 4] &= O(1). \end{aligned}$$

We define (following the guidelines of [4])

$$\begin{aligned} dci4(j) &:= \min\{|H[j-1; 4]|, |H[j-2; 4]|, |H[j-3; 4]|, |H[j-4; 4]|\}, \\ dce4(j) &:= \min\{|H[j-1; 4]|, |H[j-2; 4]|, |H[j-3; 4]|\}, \\ dni4(j) &:= \max\{|H[j; 4]|, |H[j-5; 4]|\}, \\ dne4(j) &:= \max\{|H[j; 4]|, |H[j-4; 4]|\}. \end{aligned}$$

The behavior of these quantities for the various *weak* singularities ($x_d \in (x_{j-1}, x_j]$) we want to detect is displayed in Table 5.1.

We then observe that

$$\begin{aligned} x_d = x_j &\Rightarrow h^{1/2} dce4(j) > dne4(j), \\ x_d \in (x_{j-1}, x_j) &\Rightarrow \begin{cases} h^{1/2} dci4(j) > dni4(j), \\ h^{1/2} dce4(j) > dne4(j), \quad \text{or} \\ h^{1/2} dce4(j-1) > dne4(j-1). \end{cases} \end{aligned}$$

Then, if

$$(5.1) \quad h^{1/2}dci4(j) > dni4(j), \text{ or } h^{1/2}dce4(j) > dne4(j), \\ \text{or } h^{1/2}dce4(j-1) > dne4(j-1),$$

we mark out the interval (x_{j-1}, x_j) as suspected of having a singularity in its interior. On the other hand, if

$$(5.2) \quad h^{1/2}dce4(j) > dne4(j),$$

we suspect a singularity at $x_d = x_j$.

These criteria might fail in several cases. For instance, if we have a jump at x_j ($[H'']_{x_d} = O(1)$) and $[H''']_{x_j} = 0$, it turns out that $H[j-2;4] = O(1)$ and (5.2) is not true. Also, if $x_d = x_j - \frac{4}{3}h$ and $[H']_{x_d} = 0 = [H''']_{x_d}$, $[H'']_{x_d} = O(1)$, then $dci4(j) = O(1) = dni4(j)$ and (5.1) might fail.

To avoid these problematic cases, we analyze also the fifth-order divided differences via Taylor expansions. It follows that the “exceptions” in the fourth-order divided differences are not correlated with the “exceptions” in the fifth-order divided differences. We thus propose a detection algorithm that combines the information obtained from the fourth- and fifth-order divided differences. The final algorithm is given in the appendix.

Once we have singled out the *suspicious* intervals, we must decide by using the function $G_j(x)$ if they do indeed contain a singularity.

We know that when $H(x)$ has a discontinuity in its $(m+1)$ st derivative at $x_d \in (x_{j-1}, x_j)$, it can be approximated (for sufficiently small h) by the unique root of $G_j^{(m)}(z) = q_{j+1}^{(m)}(z) - q_{j-1}^{(m)}(z) = 0$. Thus, if (x_{j-1}, x_j) is suspected of containing a singularity, we check whether

$$(5.3) \quad G_j^{(m)}(x_{j-1}) \cdot G_j^{(m)}(x_j) < 0.$$

If this is the case, we conclude that there is a root of $G_j^{(m)}(z)$ in (x_{j-1}, x_j) and we proceed with the SR technique. Otherwise, no modifications are carried out on the basic ENO reconstruction. In practice we try to identify only δ -type singularities, jumps, and corners in $f(x)$; thus, we check (5.3) for $m = 0, 1, 2$.

In our numerical experiments we found that the conditions (5.1), (5.2), together with (5.3), lead sometimes to the application of the SR technique in smooth places. A careful analysis of the functions $G_j^{(m)}(x)$ for $m = 0, 1, 2$, can help to determine whether or not a *weak* singularity lies at a *suspicious* grid point. This analysis is summarized in the appendix, together with our full detection mechanism.

6. Data compression and error control. A multiresolution representation of a discrete sequence \bar{f}^L can be viewed as a decomposition of \bar{f}^L into scales. The scale coefficients d_j^k are a combination of what we would intuitively call a *new scale*, i.e., something which is simply not predictable from lower levels of resolution, and an approximation error which depends on the *quality* of the particular reconstruction procedure that defines the prediction process.

Multiresolution representations lead naturally to data-compression algorithms. The simplest data-compression procedure is obtained by setting to zero all scale coefficients which fall below a prescribed tolerance. Let us denote

$$(6.1) \quad (\hat{d}^k)_j = \mathbf{tr}(d_j^k; \epsilon_k) = \begin{cases} 0, & |d_j^k| \leq \epsilon_k, \\ d_j^k & \text{otherwise,} \end{cases}$$

and refer to this operation as truncation. This type of data compression is used primarily to reduce the “dimensionality” of the data. A different strategy, which is used to reduce the digital representation of the data, is “quantization,” which can be modeled by

$$(6.2) \quad (\hat{d}^k)_j = \mathbf{qu}(d_j^k; \epsilon_k) = 2\epsilon_k \cdot \text{round} \left[\frac{d_j^k}{2\epsilon_k} \right],$$

where $\text{round}[\cdot]$ denotes the integer obtained by rounding. For example, if $|d_j^k| \leq 256$ and $\epsilon_k = 4$, then we can represent d_j^k by an integer which is not larger than 32 and commit a maximal error of 4. Observe that $|d_j^k| < \epsilon_k \Rightarrow \mathbf{qu}(d_j^k; \epsilon_k) = 0$ and that in both cases

$$(6.3) \quad |d_j^k - \hat{d}_j^k| \leq \epsilon_k.$$

Both strategies give us direct control over the rate of compression through an appropriate choice of the tolerance levels $\{\epsilon_k\}_{k=1}^L$. Some advantages of the compressed representation $(\bar{f}^0, \hat{d}^1, \dots, \hat{d}^L)$ are its lower storage requirements and higher transmission speeds.

By applying the inverse multiresolution transform to the compressed representation, we obtain $\hat{f}^L = M^{-1}(\bar{f}^0, \hat{d}^1, \dots, \hat{d}^L)$, an approximation to the original signal \bar{f}^L . We expect the information contents of \hat{f}^L to be very close to those of the original signal \bar{f}^L . In order for this to be true, the stability of the multiresolution scheme with respect to perturbations is essential. Studying the effect of using \hat{d}_j^k instead of d_j^k in the input of M^{-1} is equivalent to studying the effect of a perturbation in the scale coefficients in the outcome of the inverse multiresolution transform. The question of stability for linear schemes was analyzed in Part I (in the hat-average multiresolution setting). The error introduced by the perturbation in the scale coefficients in the outcome of decoding algorithm (1.4) can be estimated by analysis but cannot be directly controlled; thus, the encoding-decoding strategy given by (1.3) and (1.4) is suitable for applications where we are limited in capacity and we have to settle for whatever quality is possible under this limitation.

However, there are other applications where quality control is of utmost importance, yet we would like to be as economical as possible with respect to storage and speed of computation. Moreover, linearity is an essential ingredient in the stability analysis of Part I, and it cannot be applied to nonlinear reconstruction techniques. For the techniques developed in this paper, the question of stability with respect to perturbations needs another approach.

Given a discrete sequence \bar{f}^L and a tolerance level ϵ for accuracy, our task is to come up with a compressed representation

$$(6.4) \quad \{\bar{f}^0, \hat{d}^1, \dots, \hat{d}^L\}$$

such that if $\hat{f}^L = M^{-1}\{\bar{f}^0, \hat{d}^1, \dots, \hat{d}^L\}$, we have

$$(6.5) \quad \|\bar{f}^L - \hat{f}^L\| \leq C\epsilon$$

for an appropriate norm.

One possible way to accomplish this goal is to modify the encoding procedure in such a way that the modification allows us to keep track of the cumulative error and

truncate accordingly.

Given a tolerance level ϵ , the outcome of the modified encoding procedure should be a compressed representation (6.4) satisfying (6.5). This enables us to specify the desired level of accuracy in the decompressed signal. As to be expected, we cannot specify compression rate at the same time.

A modified encoding procedure needs to be designed keeping in mind what will be the particular decoding procedure to be used. Modified encoding procedures for the interpolatory and cell-average frameworks can be found in [7]. In what follows, we describe a modification of the encoding technique within the hat-average framework which is designed to monitor the cumulative compression error and truncate accordingly (we shall consider only truncation in this paper). We shall prove that, when used with the inverse multiresolution transform of the hat-average framework, the modification we propose satisfies (6.5) for the l^p norm with $p = \infty, 1$, and 2.

The predetermined decoding procedure is (3.18). The algorithmic description of the modified encoding is as follows:

$$\begin{aligned}
 (6.6) \quad & \text{for } k = L, \dots, 1 \\
 & \quad \text{for } j = 1, J_{k-1} - 1 \\
 & \quad \quad \bar{f}_j^{k-1} = \frac{1}{4}(\bar{f}_{2j-1}^k + 2\bar{f}_{2j}^k + \bar{f}_{2j+1}^k) \\
 & \quad \text{end} \\
 & \text{end} \\
 & \text{Set } \hat{f}^0 = \bar{f}^0 \\
 & \text{for } k = 1, \dots, L \\
 & \quad \hat{d}_{J_{k-1}}^k = \text{tr}(\bar{f}_{J_{k-1}}^k - (P_{k-1}^k \hat{f}^{k-1})_{J_{k-1}}, \epsilon_k) \\
 & \quad \hat{f}_{J_{k-1}}^k = (P_{k-1}^k \hat{f}^{k-1})_{J_{k-1}} + \hat{d}_{J_{k-1}}^k \\
 & \quad \text{for } j = J_{k-1} - 1, \dots, 1 \\
 & \quad \quad \hat{d}_j^k = \text{tr}([\bar{f}_{2j-1}^k - (P_{k-1}^k \hat{f}^{k-1})_{2j-1}] - [\bar{f}_j^{k-1} - \hat{f}_j^{k-1}], \epsilon_k) \\
 & \quad \quad \hat{f}_{2j-1}^k = (P_{k-1}^k \hat{f}^{k-1})_{2j-1} + \hat{d}_j^k \\
 & \quad \quad \hat{f}_{2j}^k = 2\hat{f}_j^{k-1} - \frac{1}{2}(\hat{f}_{2j-1}^k + \hat{f}_{2j+1}^k) \\
 & \quad \text{end} \\
 & \text{end} \\
 & \quad M^M \bar{f}^L = \{\bar{f}^0, \hat{d}^1, \dots, \hat{d}^L\}
 \end{aligned}$$

Remark 6.1. Notice that $M^{-1}(\bar{f}^0, \hat{d}^1, \dots, \hat{d}^L) = \hat{f}^L$.

PROPOSITION 6.1. *Given a discrete sequence \bar{f}^L and a tolerance level ϵ , if the truncation parameters ϵ_k in the modified encoding algorithm (6.6) are chosen so that*

$$\epsilon_k = \epsilon \cdot q^{L-k}, \quad 0 < q \leq \frac{1}{2},$$

then the sequence $\hat{f}^L = M^{-1}\{\bar{f}^0, \hat{d}^1, \dots, \hat{d}^L\}$ satisfies

$$(6.7) \quad \|\bar{f}^L - \hat{f}^L\|_p \leq C\epsilon, \quad C = \begin{cases} (1-2q)^{-1}\epsilon, & 0 < q < 1/2, \\ L\epsilon, & q = 1/2 \end{cases}$$

for $p = \infty, 1$, and 2.

Proof. Let us define the cumulative compression error at the k th level by \mathcal{E}_j^k ,

$$(6.8) \quad \mathcal{E}_j^k = \bar{f}_j^k - \hat{f}_j^k,$$

and the modified prediction error at the k th level by e_j^k ,

$$(6.9) \quad e_j^k = \bar{f}_j^k - (P_{k-1}^k \hat{f}^{k-1})_j.$$

Notice that for each $j = 1, \dots, J_{k-1} - 1$,

$$(6.10) \quad \mathcal{E}_{2j-1}^k = e_{2j-1}^k - \text{tr}(e_{2j-1}^k - \mathcal{E}_j^{k-1}, \epsilon_k).$$

Thus

$$\begin{aligned} |e_{2j-1}^k - \mathcal{E}_j^{k-1}| &> \epsilon_k \Rightarrow \mathcal{E}_{2j-1}^k = \mathcal{E}_j^{k-1}, \\ |e_{2j-1}^k - \mathcal{E}_j^{k-1}| &\leq \epsilon_k \Rightarrow \mathcal{E}_{2j-1}^k = e_{2j-1}^k = e_{2j-1}^k - \mathcal{E}_j^{k-1} + \mathcal{E}_j^{k-1}. \end{aligned}$$

In either case, we can write

$$(6.11) \quad \mathcal{E}_{2j-1}^k = \rho_j^k + \mathcal{E}_j^{k-1}, \quad j = 1, \dots, J_{k-1} - 1$$

with

$$\rho_j^k = \begin{cases} e_{2j-1}^k - \mathcal{E}_j^{k-1} & \text{if } |e_{2j-1}^k - \mathcal{E}_j^{k-1}| \leq \epsilon_k, \\ 0 & \text{if } |e_{2j-1}^k - \mathcal{E}_j^{k-1}| > \epsilon_k. \end{cases}$$

Expression (6.10) does not hold for $j = J_{k-1}$. In this case we have

$$\mathcal{E}_{J_k-1}^k = e_{J_k-1}^k - \text{tr}(e_{J_k-1}^k, \epsilon_k).$$

Thus,

$$\begin{aligned} |e_{J_k-1}^k| &> \epsilon_k \Rightarrow |\mathcal{E}_{J_k-1}^k| = 0, \\ |e_{J_k-1}^k| &\leq \epsilon_k \Rightarrow |\mathcal{E}_{J_k-1}^k| = |e_{J_k-1}^k| \leq \epsilon_k, \end{aligned}$$

and we can write

$$(6.12) \quad \mathcal{E}_{J_k-1}^k = \rho_{J_k-1}^k = \begin{cases} e_{J_k-1}^k & \text{if } |e_{J_k-1}^k| \leq \epsilon_k, \\ 0 & \text{if } |e_{J_k-1}^k| > \epsilon_k. \end{cases}$$

Notice that

$$(6.13) \quad |\rho_j^k| \leq \epsilon_k, \quad 1 \leq j \leq J_{k-1}.$$

For the even-indexed terms, it is easy to check that

$$(6.14) \quad \mathcal{E}_{2j}^k = 2\mathcal{E}_j^{k-1} - \frac{1}{2}(\mathcal{E}_{2j-1}^k + \mathcal{E}_{2j+1}^k), \quad 1 \leq j \leq J_{k-1} - 1;$$

hence, using (6.11),

$$\begin{aligned} (6.15) \quad \mathcal{E}_{2j}^k &= 2\mathcal{E}_j^{k-1} - \frac{1}{2}[\rho_{j+1}^k + \mathcal{E}_{j+1}^{k-1} + \rho_j^k + \mathcal{E}_j^{k-1}] \\ &= \frac{3}{2}\mathcal{E}_j^{k-1} - \frac{1}{2}\mathcal{E}_{j+1}^{k-1} - \frac{1}{2}[\rho_{j+1}^k + \rho_j^k] \end{aligned}$$

for $1 \leq j \leq J_{k-1} - 2$. For $j = J_k - 2$, (6.14), (6.11), and (6.12) lead to

$$(6.16) \quad \begin{aligned} \mathcal{E}_{J_k-2}^k &= 2\mathcal{E}_{J_{k-1}-1}^{k-1} - \frac{1}{2}[\rho_{J_k-3}^k + \mathcal{E}_{J_{k-1}-1}^{k-1} + \rho_{J_k-1}^k] \\ &= \frac{3}{2}\mathcal{E}_{J_{k-1}-1}^{k-1} - \frac{1}{2}[\rho_{J_k-3}^k + \rho_{J_k-1}^k]. \end{aligned}$$

Let us prove the l^∞ bound.

Observe that (6.11) and (6.13) imply

$$(6.17) \quad |\mathcal{E}_{2j-1}^k| \leq \epsilon_k + |\mathcal{E}_j^{k-1}| \leq \|\mathcal{E}^{k-1}\|_\infty + \epsilon_k, \quad 1 \leq j \leq J_{k-1} - 1,$$

while (6.12) and (6.13) imply

$$(6.18) \quad |\mathcal{E}_{J_k-1}^k| \leq \epsilon_k.$$

For the even-indexed terms, (6.15) and (6.13) imply

$$(6.19) \quad |\mathcal{E}_{2j}^k| \leq \frac{3}{2}|\mathcal{E}_j^{k-1}| + \frac{1}{2}|\mathcal{E}_{j+1}^{k-1}| + \frac{1}{2}[\epsilon_k + \epsilon_k] \leq 2\|\mathcal{E}^{k-1}\|_\infty + \epsilon_k, \\ 1 \leq j \leq J_{k-1} - 2,$$

while (6.16) and (6.13) imply

$$|\mathcal{E}_{J_k-2}^k| \leq \frac{3}{2}|\mathcal{E}_{J_{k-1}-1}^{k-1}| + \epsilon_k \leq 2\|\mathcal{E}^{k-1}\|_\infty + \epsilon_k.$$

The last four relations imply

$$(6.20) \quad \|\mathcal{E}^k\|_\infty \leq 2\|\mathcal{E}^{k-1}\|_\infty + \epsilon_k.$$

Recalling that $\mathcal{E}^0 = 0$, we get

$$(6.21) \quad \|\mathcal{E}^L\|_\infty \leq \epsilon_L + 2\|\mathcal{E}^{L-1}\|_\infty \leq \dots \leq \sum_{l=1}^L 2^{L-l}\epsilon_l;$$

hence, taking

$$(6.22) \quad \epsilon_l = \epsilon \cdot q^{L-l}, \quad 0 < q \leq \frac{1}{2},$$

we get

$$(6.23) \quad \|\bar{f}^L - \hat{f}^L\|_\infty \leq \|\mathcal{E}^L\|_\infty \leq \begin{cases} (1-2q)^{-1}\epsilon, & 0 < q < 1/2, \\ L\epsilon, & q = 1/2. \end{cases}$$

Let us now derive the bounds for the l_1 error. We define as usual

$$\|\mathcal{E}^k\|_1 = h_k \sum_{i=1}^{J_k-1} |\mathcal{E}_i^k|.$$

Thus,

$$(6.24) \quad \|\mathcal{E}^k\|_1 = h_k \{|\mathcal{E}_{J_k-1}^k| + \sum_{i=1}^{J_{k-1}-1} [|\mathcal{E}_{2i-1}^k| + |\mathcal{E}_{2i}^k|]\}.$$

Using (6.14) we can write

$$\begin{aligned}\mathcal{E}_{2i}^k + \mathcal{E}_{2i-1}^k &= 2\mathcal{E}_i^{k-1} + \frac{1}{2}\mathcal{E}_{2i-1}^k - \frac{1}{2}\mathcal{E}_{2i+1}^k, \\ \mathcal{E}_{2i}^k - \mathcal{E}_{2i-1}^k &= 2\mathcal{E}_i^{k-1} - \frac{3}{2}\mathcal{E}_{2i-1}^k - \frac{1}{2}\mathcal{E}_{2i+1}^k.\end{aligned}$$

Then

$$\begin{aligned}|\mathcal{E}_{2i}^k| + |\mathcal{E}_{2i-1}^k| &= \max(|\mathcal{E}_{2i}^k + \mathcal{E}_{2i-1}^k|, |\mathcal{E}_{2i}^k - \mathcal{E}_{2i-1}^k|) \\ &\leq 2|\mathcal{E}_i^{k-1}| + \frac{3}{2}|\mathcal{E}_{2i-1}^k| + \frac{1}{2}|\mathcal{E}_{2i+1}^k|\end{aligned}$$

and

$$\begin{aligned}\sum_{i=1}^{J_{k-1}-1} [|\mathcal{E}_{2i-1}^k| + |\mathcal{E}_{2i}^k|] &\leq \sum_{i=1}^{J_{k-1}-1} 2|\mathcal{E}_i^{k-1}| + \frac{3}{2}|\mathcal{E}_{2i-1}^k| + \frac{1}{2}|\mathcal{E}_{2i+1}^k| \\ &\leq 2 \sum_{i=1}^{J_{k-1}-1} |\mathcal{E}_i^{k-1}| + 2 \sum_{i=1}^{J_{k-1}-1} |\mathcal{E}_{2i-1}^k| + \frac{1}{2}|\mathcal{E}_{J_{k-1}}^k|.\end{aligned}$$

Substituting in (6.24) and taking into account (6.11), (6.12), and (6.13), we get

$$\begin{aligned}\|\mathcal{E}^k\|_1 &\leq \frac{h_{k-1}}{2} \left\{ \epsilon_k + 2 \sum_{i=1}^{J_{k-1}-1} |\mathcal{E}_i^{k-1}| + 2 \sum_{i=1}^{J_{k-1}-1} \{|\mathcal{E}_i^{k-1}| + |\rho_i^k|\} + \frac{1}{2}\epsilon_k \right\} \\ &\leq \frac{h_{k-1}}{2} \left\{ \frac{3}{2}\epsilon_k + 4 \sum_{i=1}^{J_{k-1}-1} |\mathcal{E}_i^{k-1}| + 2 \sum_{i=1}^{J_{k-1}-1} \epsilon_k \right\} \\ &\leq \frac{h_{k-1}}{2} \left\{ 4 \sum_{i=1}^{J_{k-1}-1} |\mathcal{E}_i^{k-1}| + \epsilon_k \left(2J_{k-1} - 2 + \frac{3}{2} \right) \right\} \\ &\leq 2\|\mathcal{E}^{k-1}\|_1 + \epsilon_k,\end{aligned}$$

and we obtain the same bounds as in the $\|\cdot\|_\infty$ case.

To derive the l^2 bound, we simply note that for an n -vector x , one has $\|x\|_2 \leq \|x\|_1$. Thus, defining as usual

$$\|\mathcal{E}^k\|_2 = h_k \left(\sum_{i=1}^{J_{k-1}} |\mathcal{E}_i^k|^2 \right)^{1/2},$$

we have

$$\|\mathcal{E}^L\|_2 \leq \|\mathcal{E}^L\|_1 \leq \begin{cases} (1-2q)^{-1}\epsilon, & 0 < q < 1/2, \\ L\epsilon, & q = 1/2. \end{cases} \quad \square$$

If the reconstruction operators \mathcal{R}_k are linear functionals, the error-control technique we have described allows us to control the quality of the decoded data instead of the compression rate. If the reconstruction operators are nonlinear (data dependent) this algorithm guarantees the stability of the data-compression procedure, while a simpler algorithm like ((3.17),(3.18)) does not.

7. Numerical experiments. Our goal in this section is to compare the capabilities of various multiresolution based compression algorithms. Mainly, we want to demonstrate that nonlinear adaptive reconstruction techniques outperform linear ones when the incoming (discrete) signal has isolated singularities. By introducing adaptivity at the reconstruction level, we reduce the approximation error component of the scale coefficients, which leads to larger compression rates.

As in [11], we measure the compression rate by comparing the number of elements in the initial sequence to the number of *significant* elements in its multiresolution representation. Thus, we define \mathcal{D}_ϵ to be the set of indices (j, k) of the significant scale coefficients in the multiresolution representation of the original sequence, i.e.,

$$(7.1) \quad \mathcal{D}_\epsilon = \mathcal{D}_\epsilon(\bar{f}^L) = \{(j, k), \quad |d_j^k| > \epsilon_k\}.$$

Then, if we denote the number of elements in \mathcal{D}_ϵ as $|\mathcal{D}_\epsilon|$, we can evaluate the efficiency of the compression scheme by computing the ratio

$$(7.2) \quad r_c = \frac{N_L}{|\mathcal{D}_\epsilon| + N_0}.$$

We shall compare the behavior of several linear and nonlinear multiresolution schemes within the hat-average multiresolution setting. We also compare with a standard multiresolution scheme based on Daubechies orthonormal wavelets. Our comparison does not intend to be exhaustive, but we expect it will serve to illustrate our point.

The linear schemes we consider are the following:

1. Daubechies orthonormal wavelets.
2. The piecewise polynomial reconstruction of Part I [2] using a periodic extension at the boundary (see section 8.3 in Part I). It is seen in [2] that these schemes are the same as the biorthogonal wavelets of [3] with the hat function as the mother scaling function ($\tilde{N} = 2$ in the notation of [3]).
3. The piecewise polynomial reconstruction of Part I [2] with one-sided stencils at the boundaries (see section 8.3 in Part I).

The nonlinear schemes we consider are based on the ENO and ENO-SR reconstruction procedures described in sections 4 and 5. It seems appropriate to mention here that the stencil selection or the location of the singularity does not constitute additional information that needs to be stored in order to recover the original signal, since the reconstruction techniques described in sections 2, 2.2, and 4 work directly on available data. Thus, the efficiency factor (7.2) is a measure of the compression capabilities of the scheme.

In our numerical displays, each scheme is identified by an acronym: O stands for “orthonormal wavelets”; BO for “biorthogonal wavelets”; PP for the “piecewise polynomial” reconstruction described in [2] with one-sided reconstructions at the boundary, and the ENO labels are self-explanatory. The order of the reconstruction procedure follows the scheme identification name; for example, O-4 stands for orthonormal wavelets of order 4 (4 vanishing moments).

For stable (with respect to perturbations) linear multiresolution transforms, the analysis of Part I shows that if $\hat{f}^L = M^{-1} \mathbf{tr}(M \bar{f}^L) = M^{-1} \{\bar{f}^0, \hat{d}^1, \dots, \hat{d}^L\}$ with \hat{d}_j^k as in (6.1), then

$$\|\bar{f}^L - \hat{f}^L\| \leq C \sum_{k=1}^L \epsilon_k.$$

It seems thus that appropriate truncation strategies for these compression schemes should be to consider (6.1) with $\epsilon_k = \epsilon/(2^{k-L-1})$ (this would lead to bounds proportional to ϵ) or $\epsilon_k = \epsilon$ (which would lead to bounds proportional to $L\epsilon$).

For nonlinear multiresolution schemes stability is guaranteed if a modified encoding procedure such as that of (6.6) is used. In this case the error bounds are those found in Proposition 6.1.

In all our experiments the finest grid X^L is a uniform grid of $J_L = 1024$ points, and the coarsest one, X^0 , has $J_0 = 8$ points. Thus, the multiresolution schemes have $L = 7$.

In our first set of experiments, we compress a discrete set of data that is associated to a function which exhibits a singularity. To illustrate the behavior of the schemes with respect to the type of singularity we shall consider three examples, each one displaying singularities of different strength.

The *kink function*, written as

$$(7.3) \quad f_1(x) = \left| \sin \left(\frac{3}{2} \pi \left(x - \frac{1}{2} \right) \right) \right|, \quad x \in [0, 1].$$

The *step function*, written as

$$(7.4) \quad f_2(x) = \begin{cases} \frac{1}{2} \sin(\pi x), & x \leq \frac{2}{3}, \\ \frac{1}{2} - \sin(\pi x), & x > \frac{2}{3}. \end{cases}$$

The δ -*function*, written as

$$(7.5) \quad f_3(x) = \sin \left(\frac{\pi}{4} x \right) + \delta(x - x_{741}) + \frac{1}{1024} \delta(x - x_{241}).$$

We obtain the discrete data by considering point values of $f_1(x)$ and $f_2(x)$ on the grid X^L ; the discrete data associated with $f_3(x)$ are also its point values on the grid X^L except for $\bar{f}_{241} = \sin(\frac{\pi}{4} x_{241}) + 1$ and $\bar{f}_{741} = \sin(\frac{\pi}{4} x_{741}) + 1024$. The discrete data are displayed in the leftmost corner of Figures 7.1, 7.2, and 7.3 (for $f_3(x)$, only the smooth part and the small δ are displayed; the $O(1)$ - δ is off the scale).

In our numerical study we compute, for a given truncation strategy, the efficiency factor (7.2) as well as the errors $\|\bar{f}^L - \hat{f}^L\|_p$ for $p = 1, 2$, and ∞ for each of the schemes we consider. These results, along with the truncation strategy chosen, are compiled in Tables 7.1, 7.2, 7.3, 7.4, 7.5, and 7.6.

The main conclusions we can extract from these tables are the following:

1. Nonlinear techniques improve the compression rates while ensuring an adequate quality in the decompressed signal. As expected, reducing the low-accuracy region in the reconstruction step improves the compression properties of the scheme.
2. The stronger the singularity, the larger the increment in compression capabilities of nonlinear schemes with respect to linear ones.
3. For linear schemes, the $\epsilon_k = \epsilon$ and $\epsilon_k = \epsilon/2^{L-k+1}$ strategies lead to essentially the same results. The errors in Tables 7.4, 7.5, and 7.6 are slightly smaller than those in Tables 7.1, 7.2, and 7.3, but the corresponding compression rate is slightly smaller too. Similar results can be obtained by increasing ϵ in the $\epsilon_k = \epsilon$ strategy.
4. For nonlinear schemes, the strategy $\epsilon_k = \epsilon/2^{L-k+1}$ always leads to numerical errors which are smaller than ϵ , although the theoretical bound is $L\epsilon/2$. A

TABLE 7.1
Kink function.

Method	r_c	L_∞ -error	L_1 -error	L_2 -error	ϵ_k
O-4	17.36	$5.24 \cdot 10^{-4}$	$2.91 \cdot 10^{-5}$	$1.91 \cdot 10^{-6}$.001
BO-4	26.95	$2.50 \cdot 10^{-3}$	$2.56 \cdot 10^{-4}$	$1.31 \cdot 10^{-5}$.001
PP-4	34.10	$2.35 \cdot 10^{-3}$	$3.18 \cdot 10^{-4}$	$1.46 \cdot 10^{-5}$.001
ENO-4	23.79	$5.36 \cdot 10^{-3}$	$6.80 \cdot 10^{-5}$	$8.06 \cdot 10^{-6}$	$.01/2^{L-k+1}$
ENO-5	33.00	$4.77 \cdot 10^{-3}$	$3.95 \cdot 10^{-5}$	$6.14 \cdot 10^{-6}$	$.01/2^{L-k+1}$
ENO-SR-4	31.97	$3.50 \cdot 10^{-3}$	$3.77 \cdot 10^{-5}$	$6.00 \cdot 10^{-6}$	$.01/2^{L-k+1}$
ENO-SR-5	56.83	$8.80 \cdot 10^{-3}$	$4.25 \cdot 10^{-5}$	$6.37 \cdot 10^{-6}$	$.01/2^{L-k+1}$

TABLE 7.2
Step function.

Method	r_c	L_∞ -error	L_1 -error	L_2 -error	ϵ_k
O-4	13.65	$2.89 \cdot 10^{-4}$	$1.36 \cdot 10^{-5}$	$9.98 \cdot 10^{-7}$.001
BO-4	15.06	$8.86 \cdot 10^{-4}$	$7.86 \cdot 10^{-5}$	$5.70 \cdot 10^{-6}$.001
PP-4	23.79	$2.83 \cdot 10^{-3}$	$2.09 \cdot 10^{-4}$	$1.33 \cdot 10^{-5}$.001
ENO-4	31.00	$7.64 \cdot 10^{-4}$	$3.68 \cdot 10^{-5}$	$5.93 \cdot 10^{-6}$	$.01/2^{L-k+1}$
ENO-5	27.65	$8.47 \cdot 10^{-5}$	$2.73 \cdot 10^{-6}$	$1.62 \cdot 10^{-6}$	$.01/2^{L-k+1}$
ENO-SR-4	42.62	$4.27 \cdot 10^{-3}$	$9.66 \cdot 10^{-5}$	$9.61 \cdot 10^{-6}$	$.01/2^{L-k+1}$
ENO-SR-5	44.48	$4.94 \cdot 10^{-3}$	$3.64 \cdot 10^{-5}$	$5.89 \cdot 10^{-6}$	$.01/2^{L-k+1}$

TABLE 7.3
 δ -function.

Method	r_c	L_∞ -error	L_1 -error	L_2 -error	ϵ_k
O-4	9.57	$3.34 \cdot 10^{-4}$	$1.70 \cdot 10^{-5}$	$1.36 \cdot 10^{-6}$.001
BO-4	10.56	$2.02 \cdot 10^{-3}$	$2.05 \cdot 10^{-5}$	$3.97 \cdot 10^{-6}$.001
PP-4	13.64	$2.07 \cdot 10^{-3}$	$1.24 \cdot 10^{-4}$	$1.11 \cdot 10^{-5}$.001
ENO-4	24.95	$3.30 \cdot 10^{-3}$	$2.19 \cdot 10^{-5}$	$4.58 \cdot 10^{-6}$	$.01/2^{L-k+1}$
ENO-5	24.95	$5.28 \cdot 10^{-3}$	$5.34 \cdot 10^{-5}$	$7.14 \cdot 10^{-6}$	$.01/2^{L-k+1}$
ENO-SR-4	36.53	$2.08 \cdot 10^{-3}$	$1.41 \cdot 10^{-5}$	$3.67 \cdot 10^{-6}$	$.01/2^{L-k+1}$
ENO-SR-5	37.89	$5.45 \cdot 10^{-3}$	$2.60 \cdot 10^{-5}$	$4.99 \cdot 10^{-6}$	$.01/2^{L-k+1}$

TABLE 7.4
Kink-function ϵ_k -strategies.

Method	r_c	L_∞ -error	L_1 -error	L_2 -error	ϵ_k
O-4	17.96	$1.63 \cdot 10^{-3}$	$2.81 \cdot 10^{-5}$	$3.85 \cdot 10^{-6}$	$.01/2^{L-k+1}$
BO-4	22.26	$2.50 \cdot 10^{-3}$	$7.80 \cdot 10^{-5}$	$8.55 \cdot 10^{-6}$	$.01/2^{L-k+1}$
PP-4	25.57	$2.25 \cdot 10^{-3}$	$5.30 \cdot 10^{-5}$	$6.01 \cdot 10^{-6}$	$.01/2^{L-k+1}$
ENO-4	14.41	$8.55 \cdot 10^{-4}$	$9.90 \cdot 10^{-5}$	$3.08 \cdot 10^{-6}$	$.01/4^{L-k+1}$
ENO-5	22.73	$4.17 \cdot 10^{-4}$	$4.86 \cdot 10^{-6}$	$2.16 \cdot 10^{-6}$	$.01/4^{L-k+1}$
ENO-SR-4	17.05	$7.37 \cdot 10^{-5}$	$3.26 \cdot 10^{-6}$	$1.76 \cdot 10^{-6}$	$.01/4^{L-k+1}$
ENO-SR-5	34.10	$5.40 \cdot 10^{-4}$	$2.33 \cdot 10^{-6}$	$1.49 \cdot 10^{-6}$	$.01/4^{L-k+1}$
ENO-SR-6	31.00	$9.52 \cdot 10^{-4}$	$4.08 \cdot 10^{-6}$	$1.97 \cdot 10^{-6}$	$.01/4^{L-k+1}$

strategy like $\epsilon_k = \epsilon/4^{L-k+1}$ leads to a moderate decrease in the compression rate and an improvement (of an order of magnitude or more) in the numerical errors in the l^∞ and l^1 norms. It also improves the effectiveness of the SR technique (see Figure 7.5).

TABLE 7.5
Step-function ϵ_k -strategies.

Method	r_c	L_∞ -error	L_1 -error	L_2 -error	ϵ_k
O-4	13.65	$5.61 \cdot 10^{-4}$	$1.31 \cdot 10^{-5}$	$1.24 \cdot 10^{-6}$	$.01/2^{L-k+1}$
BB-4	14.84	$9.86 \cdot 10^{-5}$	$1.54 \cdot 10^{-5}$	$8.04 \cdot 10^{-7}$	$.01/2^{L-k+1}$
PP-4	22.73	$4.29 \cdot 10^{-4}$	$2.99 \cdot 10^{-5}$	$1.81 \cdot 10^{-6}$	$.01/2^{L-k+1}$
ENO-4	22.24	$3.57 \cdot 10^{-5}$	$2.40 \cdot 10^{-6}$	$1.51 \cdot 10^{-6}$	$.01/4^{L-k+1}$
ENO-5	26.23	$3.12 \cdot 10^{-5}$	$1.15 \cdot 10^{-6}$	$1.05 \cdot 10^{-6}$	$.01/4^{L-k+1}$
ENO-SR-4	28.42	$4.42 \cdot 10^{-4}$	$4.30 \cdot 10^{-6}$	$2.03 \cdot 10^{-6}$	$.01/4^{L-k+1}$
ENO-SR-5	37.89	$1.96 \cdot 10^{-3}$	$5.29 \cdot 10^{-6}$	$2.25 \cdot 10^{-6}$	$.01/4^{L-k+1}$
ENO-SR-6	42.62	$3.28 \cdot 10^{-4}$	$1.41 \cdot 10^{-6}$	$1.16 \cdot 10^{-6}$	$.01/4^{L-k+1}$

TABLE 7.6
 δ -function ϵ_k -strategies.

Method	r_c	L_∞ -error	L_1 -error	L_2 -error	ϵ_k
O-4	9.39	$3.43 \cdot 10^{-4}$	$6.87 \cdot 10^{-6}$	$8.01 \cdot 10^{-7}$	$.01/2^{L-k+1}$
BO-4	10.56	$2.02 \cdot 10^{-3}$	$2.05 \cdot 10^{-5}$	$3.97 \cdot 10^{-6}$	$.01/2^{L-k+1}$
PP-4	13.29	$2.02 \cdot 10^{-3}$	$2.05 \cdot 10^{-5}$	$3.97 \cdot 10^{-6}$	$.01/2^{L-k+1}$
ENO-4	24.95	$2.45 \cdot 10^{-5}$	$1.75 \cdot 10^{-7}$	$4.09 \cdot 10^{-7}$	$.01/4^{L-k+1}$
ENO-5	24.95	$3.45 \cdot 10^{-6}$	$1.81 \cdot 10^{-8}$	$1.31 \cdot 10^{-7}$	$.01/4^{L-k+1}$
ENO-SR-4	37.89	$3.51 \cdot 10^{-4}$	$8.14 \cdot 10^{-7}$	$8.82 \cdot 10^{-7}$	$.01/4^{L-k+1}$
ENO-SR-5	39.35	$2.27 \cdot 10^{-4}$	$5.49 \cdot 10^{-7}$	$7.24 \cdot 10^{-7}$	$.01/4^{L-k+1}$
ENO-SR-6	39.35	$6.05 \cdot 10^{-6}$	$1.22 \cdot 10^{-8}$	$1.08 \cdot 10^{-7}$	$.01/4^{L-k+1}$

It is also very interesting to display the *location* of the nonzero scale coefficients. In Figures 7.1, 7.2, 7.3, 7.4, 7.5, and 7.6, a circle is drawn around (j, k) for each d_j^k above the tolerance ϵ_k . It is easy to observe that the prediction process for each multiresolution scheme does a good job at predicting information on smooth portions of the signal; however, the behavior around a singularity is quite different.

Each singularity has associated a *signature* in each one of the multiresolution schemes. The signature essentially measures the extent of the low-accuracy regions for the reconstruction process that defines the prediction.

It is easy to see that the signature of the different types of singularities is practically the same for linear schemes. If periodicity is assumed, there is also the *boundary signature*, i.e., the signature corresponding to the singularity introduced by the periodicity assumption. As expected, the boundary signature is eliminated when using the multiresolution scheme for bounded domains labeled PP.

Some of our remarks in section 5 can also be observed by looking at these displays. In particular, we observe that the ENO stencil selection process might be fooled by weak singularities. In Figure 7.1 we see that the signature of the corner in the ENO scheme is similar to that of the linear schemes. However, the signature completely disappears when the SR technique is used. This indicates that the detection mechanism we describe in the appendix as well as the SR technique both work appropriately. The corner in Figure 7.1 is located at the center of the interval, and the influence of the one-sided reconstructions at the boundary is not felt until the coarsest level is attained. The behavior of the schemes for a step discontinuity or a *small* δ at this location is the same (not displayed). In fact, the pattern of nonzero elements is about the same in all the singularities we study, if their initial location in the finest grid is the same. For an $O(1)$ δ , the ENO reconstruction considers stencils from only the

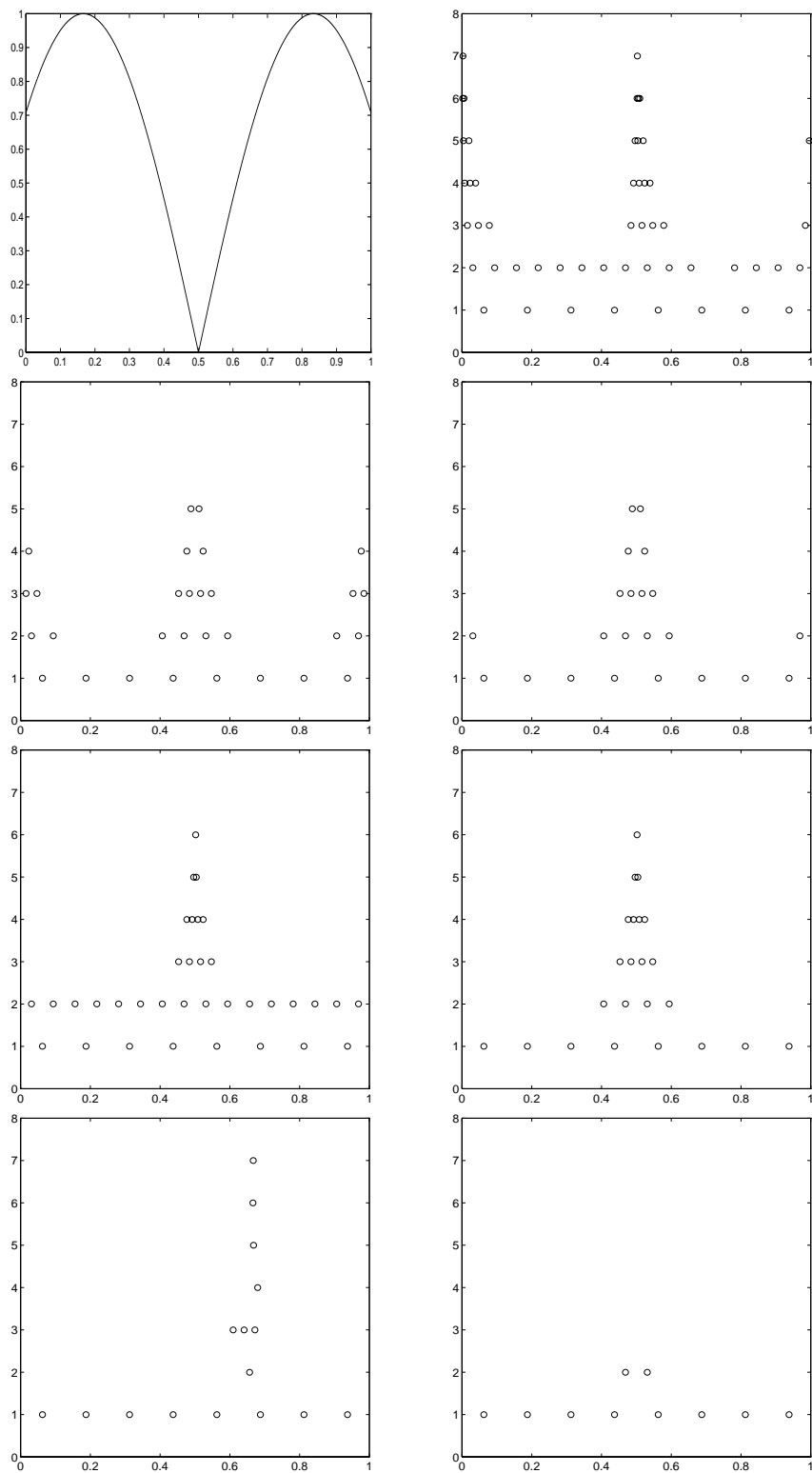


FIG. 7.1. Top to bottom and left to right: kink function, O-4; BO-4; PP-4; ENO-4, ENO-5; ENO-SR-4; ENO-SR-5; ϵ_k as in Table 7.1.

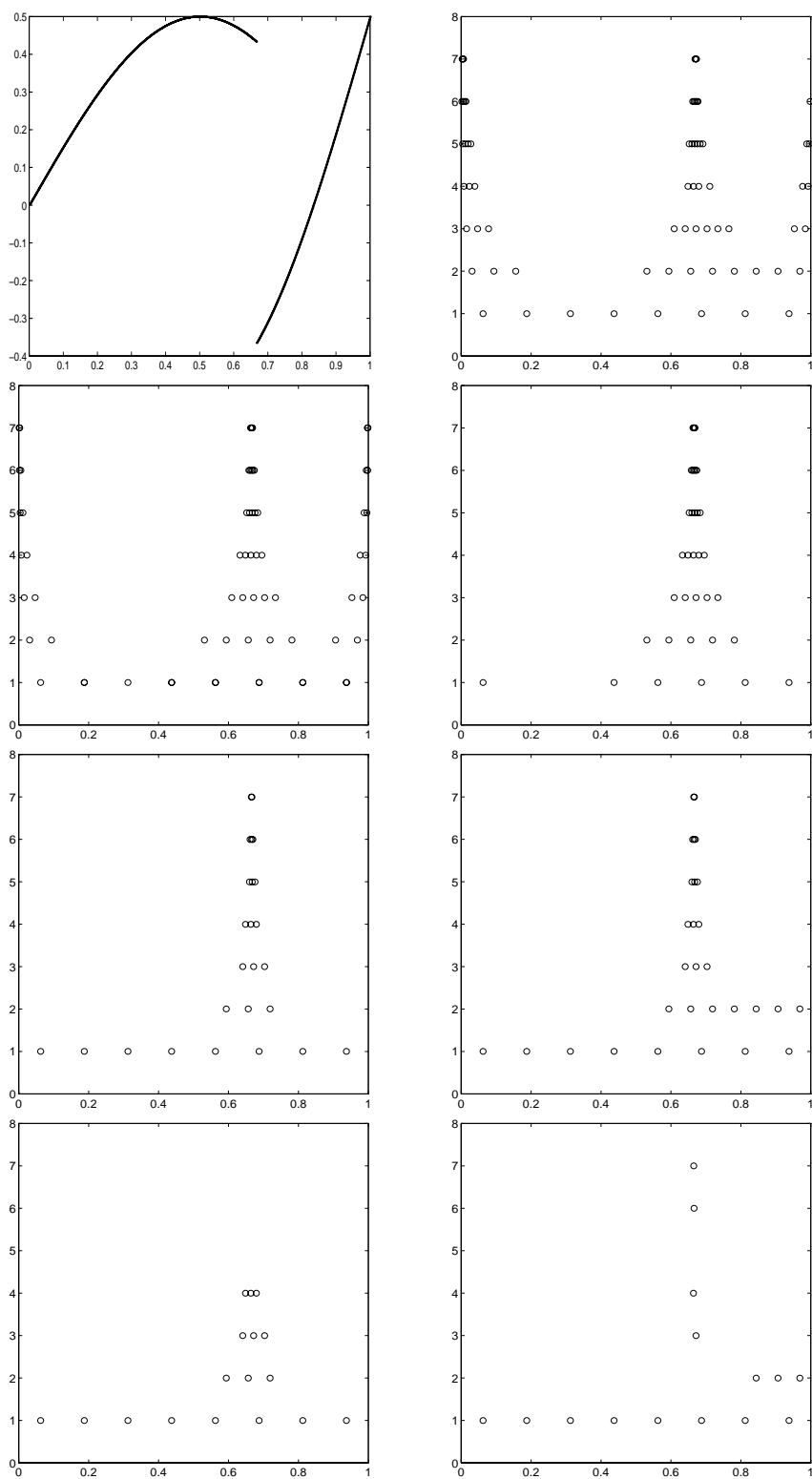


FIG. 7.2. Top to bottom and left to right: step function, $O-4$; $BO-4$, $PP-4$; $ENO-4$, $ENO-5$; $ENO-SR-4$, $ENO-SR-5$; ϵ_k as in Table 7.2.

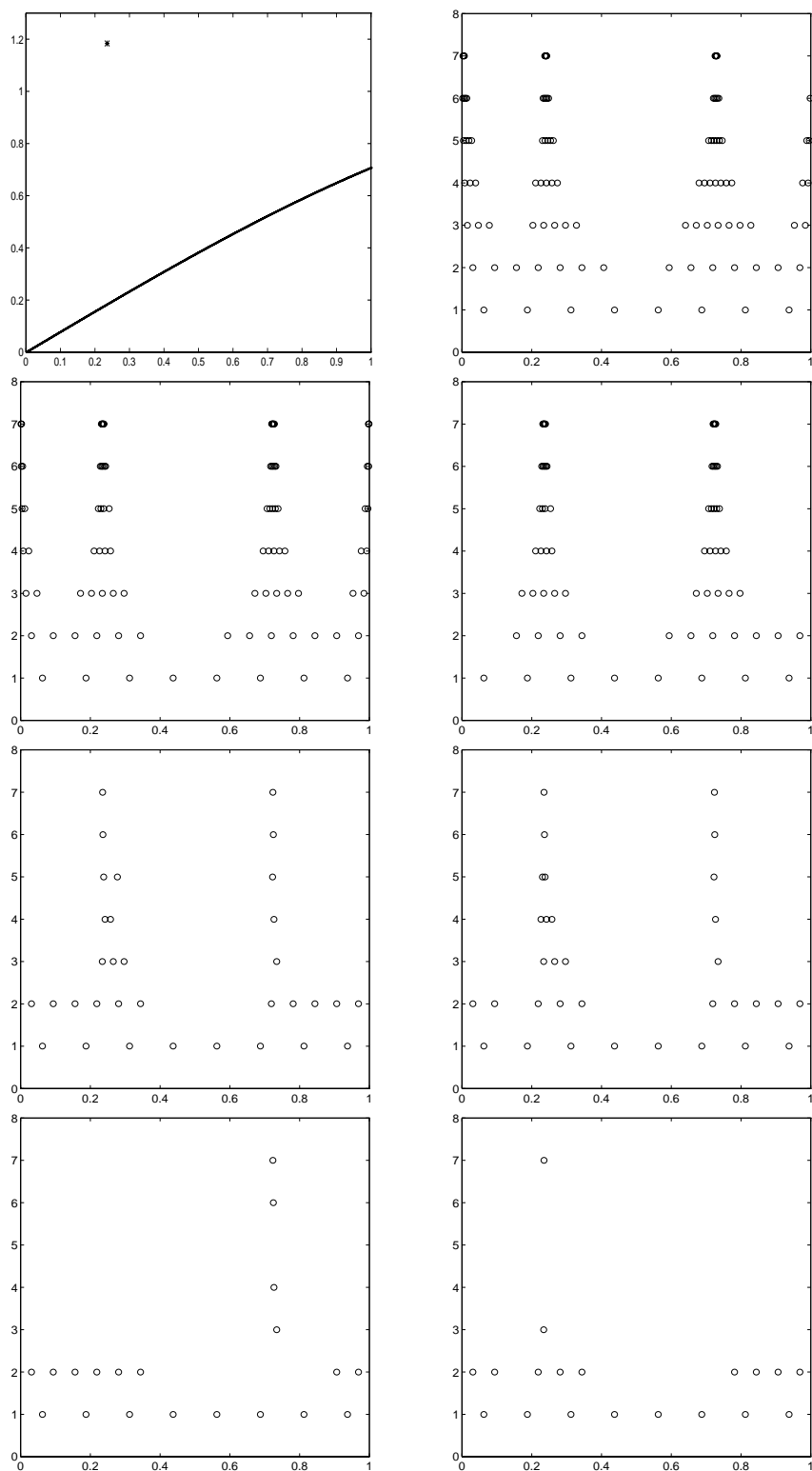


FIG. 7.3. Top to bottom and left to right: δ function, O-4; BO-4, PP-4; ENO-4, ENO-5; ENO-SR-4, ENO-SR-5; ϵ_k as in Table 7.3.

TABLE 7.7
Harten's function.

Method	r_c	L_∞ -error	L_1 -error	L_2 -error	ϵ_k
O-4	6.65	$3.42 \cdot 10^{-4}$	$2.90 \cdot 10^{-5}$	$1.57 \cdot 10^{-6}$.001
BO-4	7.47	$2.15 \cdot 10^{-3}$	$2.51 \cdot 10^{-4}$	$1.40 \cdot 10^{-5}$.001
PP-4	8.60	$2.98 \cdot 10^{-3}$	$3.38 \cdot 10^{-4}$	$1.79 \cdot 10^{-5}$.001
ENO-4	10.13	$4.39 \cdot 10^{-3}$	$1.19 \cdot 10^{-4}$	$1.07 \cdot 10^{-5}$	$.01/2^{L-k+1}$
ENO-5	10.44	$3.36 \cdot 10^{-3}$	$7.72 \cdot 10^{-5}$	$8.59 \cdot 10^{-6}$	$.01/2^{L-k+1}$
ENO-SR-4	13.64	$4.85 \cdot 10^{-3}$	$2.05 \cdot 10^{-4}$	$1.40 \cdot 10^{-5}$	$.01/2^{L-k+1}$
ENO-SR-5	15.74	$4.86 \cdot 10^{-3}$	$8.38 \cdot 10^{-5}$	$8.95 \cdot 10^{-6}$	$.01/2^{L-k+1}$

smooth side of the function and the signature is, also, basically eliminated.

To observe the boundary effects, we have located the jump discontinuity in $f_2(x)$ closer to the right boundary. Figure 7.2 shows the pattern of nonzero scale coefficients in this case. We see that the one-sided reconstruction procedures, together with the truncation strategy imposed by the modified encoding algorithm, lead to a nonempty signature at the discontinuity even when applying the SR technique. We have observed that our detection mechanism always locates the singularity, but the approximation properties of the one-sided reconstructions might not be good enough to eliminate completely the signature in the coarsest levels. Then, the (highly localized) perturbations are carried back to higher resolution levels by the modified encoding algorithm (recall that the detection mechanism and the ENO-SR reconstruction work on available data, and the computation of the approximate location of the singularity is based on those data).

Since this framework allows us to choose a different reconstruction technique at each resolution level, we could, in principle, apply the SR technique only up to a certain level. For the step-function, we can obtain absolute compression up to level 4 for $p = 4$ and up to level 2 for $p = 5$ (see Figure 7.4); however, the compression rate and the errors are basically unchanged.

In Figure 7.3 we superimpose two δ -functions of different strengths to an underlying smooth signal. We observe a difference in the way the ENO technique deals with the $O(1)$ and $O(h_L)$ δ -singularities. The signature of the $O(1)$ - δ is just one point, but the *small* δ does fool the hierarchical stencil selection algorithm, producing poorer approximations and, in turn, a wider signature than in the $O(1)$ case. As before, the nonempty signature in the SR case is a result of the proximity of the singularity to the boundary. It can also be eliminated by applying the SR technique on a limited number of levels (starting from the finest).

To finish, we consider Harten's function, with the addition of a *small* δ ,

$$f_4(x) = \frac{1}{1024} \delta(x - x_{865}) + \begin{cases} -x \sin(\frac{3\pi}{2} x^2), & -1 < x \leq -\frac{1}{3}, \\ |\sin(2\pi x)|, & |x| < \frac{1}{3}, \\ 2x - 1 - \sin(3\pi x)/6, & \frac{1}{3} \leq x < 1. \end{cases}$$

Figure 7.6 displays the discrete input data and the pattern of nonzero scale coefficients corresponding to the numerical experiments in Table 7.7.

The number of singularities present in this function make it an interesting test for compression methods. As before, the ENO-SR method attains the highest compression rate while keeping the error below the specified tolerance.

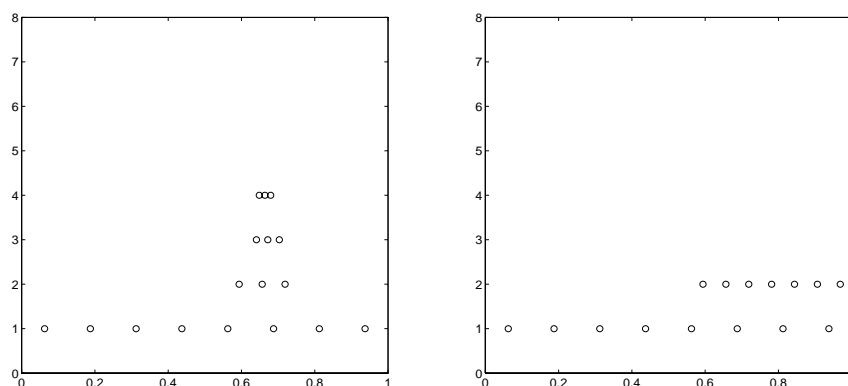


FIG. 7.4. Step-function; left: ENO-SR-4 SR only up to level 5; right: ENO-SR-5 SR only up to level 3.

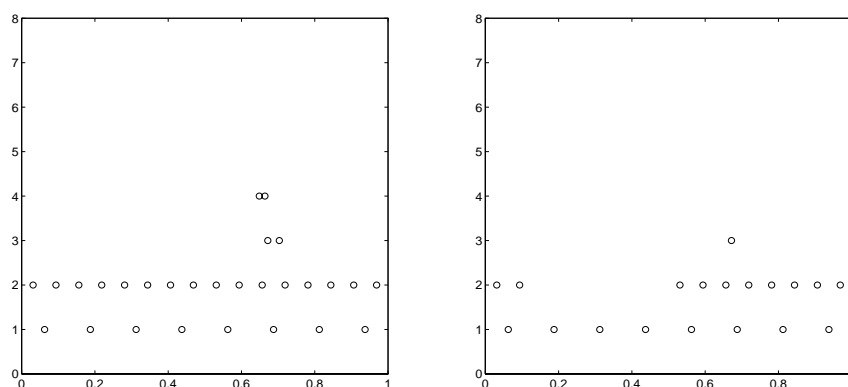


FIG. 7.5. Step-function; left: ENO-SR-4; right: ENO-SR-5 $\epsilon_k = \epsilon/4^{L-k+1}$.

We would like to mention that another option for the design of the compression algorithm, which we have not explored in this paper, is to determine the location of the singularity at the finest resolution level and store this information to use it at all levels of resolution and in the inverse multiresolution transform.

8. Summary and conclusions. In [7, 8, 9], Harten introduces a general framework for multiresolution schemes based on two operators: decimation (always linear) and prediction (linear or nonlinear).

In [2] and this paper we consider the decimation operator which is derived from the discretization process of taking local averages with respect to the hat function.

In the first paper in the series, [2], we considered linear prediction operators based on centered interpolation and studied the stability properties of the resulting multiresolution schemes. Here we consider nonlinear prediction operators based on ENO interpolation. We design a modified encoding algorithm within the hat-weighted framework that keeps track of the cumulative error and leads to stable multiresolution schemes even for nonlinear prediction operators.

In the hat-multiresolution context, the ENO technique allows us to detect δ -type singularities. One can then use Harten's SR technique to improve the accuracy of the

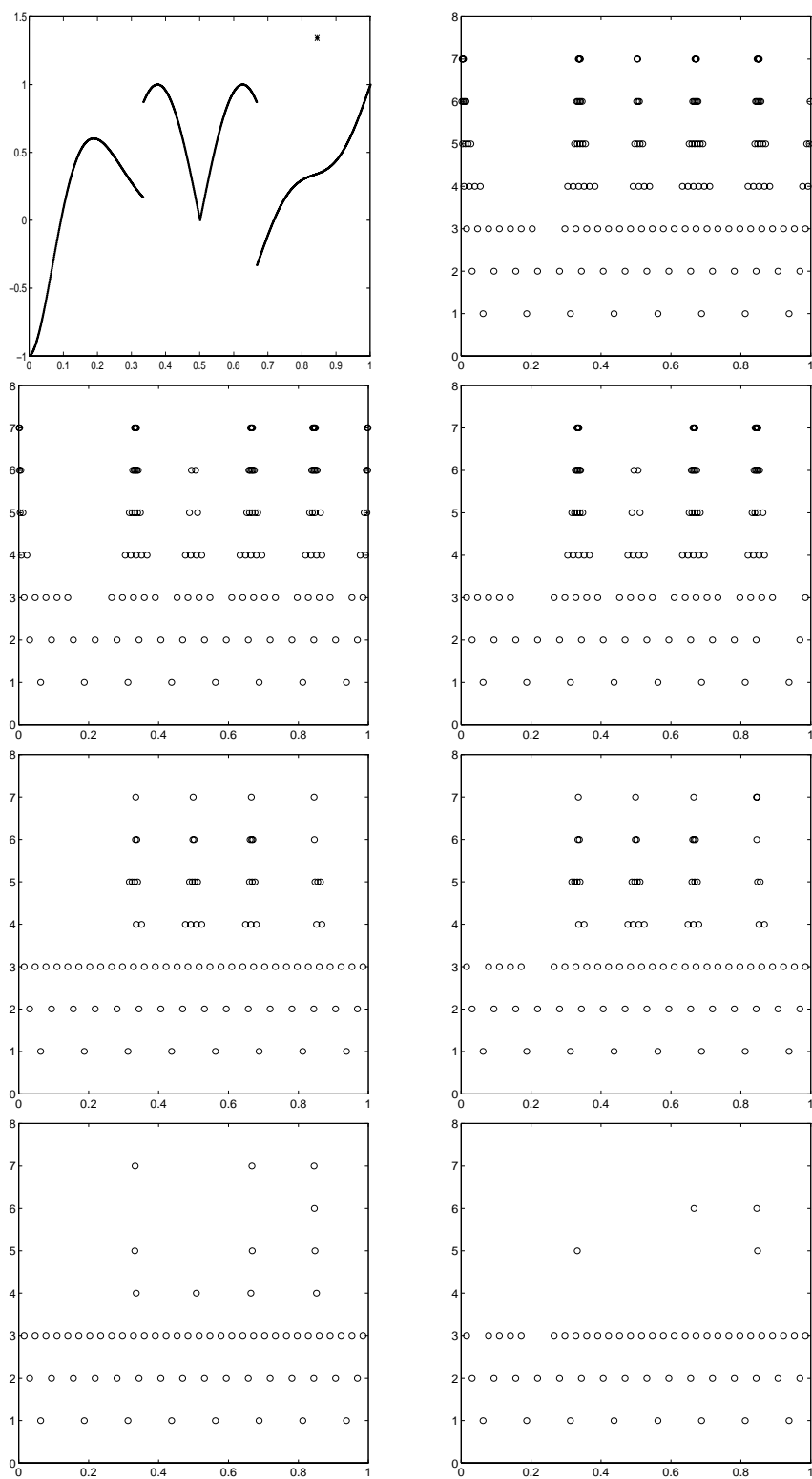


FIG. 7.6. Top to bottom and left to right: Harten's function, O-4; BO-4; PP-4; ENO-4; ENO-5; ENO-SR-4; ENO-SR-5.

TABLE 7.8
 δ -type singularity in $f(x)$ ($[H']_{x_d} \neq 0$).

	$x_d \in (x_{j-1}, x_j)$		$x_d = x_j$	
z	$G_j(z)$	$G'_j(z)$	$G_j(z)$	$G'_j(z)$
x_{j-1}	$(a-1)h[H']_{x_d}$	$[H']_{x_d}$	$-h[H']_{x_d}$	$[H']_{x_d}$
x_j	$ah[H']_{x_d}$	$[H']_{x_d}$	$O(h^{p+2})$	$[H']_{x_d}$
x_{j+1}	$(a+1)h[H']_{x_d}$	$[H']_{x_d}$	$h[H']_{x_d}$	$[H']_{x_d}$

TABLE 7.9
 Jump in $f(x)$ ($[H'']_{x_d} \neq 0$).

	$x_d \in (x_{j-1}, x_j)$		$x_d = x_j$	
z	$G'_j(z)$	$G''_j(z)$	$G'_j(z)$	$G''_j(z)$
x_{j-1}	$(a-1)h[H'']_{x_d}$	$[H'']_{x_d}$	$-h[H'']_{x_d}$	$[H'']_{x_d}$
x_j	$ah[H'']_{x_d}$	$[H'']_{x_d}$	$O(h^{p+1})$	$[H'']_{x_d}$
x_{j+1}	$(a+1)h[H'']_{x_d}$	$[H'']_{x_d}$	$h[H'']_{x_d}$	$[H'']_{x_d}$

TABLE 7.10
 Corner in $f(x)$ ($[H''']_{x_d} \neq 0$).

	$x_d \in (x_{j-1}, x_j)$		$x_d = x_j$	
z	$G'_j(z)$	$G''_j(z)$	$G'_j(z)$	$G''_j(z)$
x_{j-1}	$\frac{1}{2}(a-1)^2h^2[H''']_{x_d}$	$(a-1)h[H''']_{x_d}$	$\frac{1}{2}h^2[H''']_{x_d}$	$-h[H''']_{x_d}$
x_j	$\frac{1}{2}a^2h^2[H''']_{x_d}$	$ah[H''']_{x_d}$	$O(h^{p+1})$	$O(h^p)$
x_{j+1}	$\frac{1}{2}(a+1)^2h^2[H''']_{x_d}$	$(a+1)h[H''']_{x_d}$	$\frac{1}{2}h^2[H''']_{x_d}$	$h[H''']_{x_d}$

prediction. We also design a more elaborate detection mechanism that allows us to apply the SR technique to jump-discontinuities and to discontinuities in the derivative of the original signal (corners).

Our numerical experiments confirm our theoretical observations: The nonlinear schemes always give higher compression rates than the linear ones. Highest compression occurs at resolution levels for which the singularities are well separated, i.e., it is possible to choose a stencil for the interpolating polynomials that stays within a region of smoothness of the original signal.

Appendix I: The detection mechanism. We shall now describe the strategy we use to determine whether or not the SR technique should be applied at a given cell. Our mechanism also detects a singularity at a grid point. After wide experimentation, we confirm that our strategy successfully detects δ -type singularities (of $O(1)$ strength as well as those labeled “small”), jumps, and corners in the (discrete) incoming signal.

As mentioned in section 5, we use the fourth- and fifth-order divided differences to isolate first those cells which exhibit “nonsmooth” behavior.

For each $j \geq 1$, define

$$\begin{aligned}
 dci4(j) &:= \min(|H[j-1;4]|, |H[j-2;4]|, |H[j-3;4]|, |H[j-4;4]|), \\
 dce4(j) &:= \min(|H[j-1;4]|, |H[j-2;4]|, |H[j-3;4]|), \\
 dni4(j) &:= \max(|H[j;4]|, |H[j-5;4]|),
 \end{aligned}$$

$$dne4(j) := \max(|H[j; 4]|, |H[j - 4; 4]|)$$

and evaluate

$$\begin{aligned} dci5(j) &:= \min(|H[j - 1; 5]|, |H[j - 2; 5]|, |H[j - 3; 5]|, |H[j - 4; 5]|, |H[j - 5; 5]|), \\ dce5(j) &:= \min(|H[j - 1; 5]|, |H[j - 2; 5]|, |H[j - 3; 5]|, |H[j - 4; 5]|), \\ dni5(j) &:= \max(|H[j; 5]|, |H[j - 6; 5]|), \\ dne5(j) &:= \max(|H[j; 5]|, |H[j - 5; 5]|). \end{aligned}$$

We use this information (see section 5) to decide if the cell is suspected of containing a discontinuity. Then, if

$$(A.1) \quad \begin{cases} h^{1/2}dce4(j) > dne4(j) & \text{or} \\ h^{1/2}dce5(j) > dne5(j), \end{cases}$$

there is a possible singularity at x_j , and if

$$(A.2) \quad \begin{cases} h^{1/2}dci4(j) > dni4(j), \\ h^{1/2}dci5(j) > dni5(j), \\ h^{1/2}dce4(j) > dne4(j), \\ h^{1/2}dce5(j) > dne5(j), \\ h^{1/2}dce4(j-1) > dne4(j-1), & \text{or} \\ h^{1/2}dce5(j-1) > dne5(j-1), \end{cases}$$

there is a possible singularity in (x_{j-1}, x_j) .

The second step is to use the function $G_j(x)$ and its derivatives to confirm the presence of a singularity.

In our numerical experiments we found that the sign change condition (5.3) leads sometimes to the application of the SR technique in smooth places. Tables 7.8, 7.9, and 7.10 (which are constructed via Taylor expansions) reflect the behavior of the functions $G^{(m)}$ near the three types of singularities we want to identify. Using the information in these tables we add more conditions to the definition of a *singular* cell.

For instance, let us assume that we have a corner. From Table 7.10 we can see that if the corner is located at x_j , then

$$(A.3) \quad \begin{cases} G_j''(x_{j+1})G_j''(x_{j-1}) \leq 0, \\ |G_j''(x_j)| \leq \min(|G_j''(x_{j-1})|, |G_j''(x_{j+1})|)h^{\frac{1}{2}}, \\ G_j'(x_{j+1})G_j'(x_{j-1}) \geq 0, \\ |G_j'(x_{j+1})| < |G_j'(x_{j-1})|, & \text{and} \\ |G_j'(x_{j-1})| < |G_j'(x_{j+1})|. \end{cases}$$

Also, if the corner is in (x_{j-1}, x_j) , then

$$(A.4) \quad \begin{cases} G_j''(x_j)G_j''(x_{j-1}) < 0, \\ \min(|G_j''(x_{j-1})|, |G_j''(x_j)|) \geq h^2, \\ 0 \leq \min(G_j'(x_{j-1})G_j'(x_j), G_j'(x_{j+1})G_j'(x_j)), \\ |G_j'(x_j)| < |G_j'(x_{j-1})|, & \text{and} \\ |G_j'(x_{j-1})| < |G_j'(x_{j+1})|. \end{cases}$$

Although the conditions (A.3) and (A.4) do not imply that there is a corner, in our numerical experiments we find that they effectively filter out fake singularities. The

```

ave := (|G'(x_{j-1})| + |G'(x_j)| + |G'(x_{j+1})|)/3
nn = 0
if (h^{1/2}dce4(j) > dne4(j) or h^{1/2}dce5(j) > dne5(j)) then
  if (G'_j(x_{j-1})G'_j(x_{j+1}) ≤ 0 and |G'_j(x_j)| ≤ h min(|G'_j(x_{j-1})|, |G'_j(x_{j+1})|)
    and 0 ≤ min(G'_j(x_{j-1})G''_j(x_j), G'_j(x_{j+1})G''_j(x_j)) and |G'_j(x_{j+1})| < |G''_j(x_{j+1})|
    and |G'_j(x_{j-1})| < |G''_j(x_{j-1})|) then
    there is a jump at x_j
    nn = 1
  elseif (G''_j(x_{j+1})G''_j(x_{j-1}) ≤ 0 and |G''_j(x_j)| ≤ h^{1/2} min(|G''_j(x_{j-1})|, |G''_j(x_{j+1})|)
    and G'_j(x_{j+1})G'_j(x_{j-1}) ≥ 0 and |G'_j(x_{j+1})| < |G''_j(x_{j+1})|
    and |G'_j(x_{j-1})| < |G''_j(x_{j-1})|) then
    there is a corner at x_j
    nn = 1
  elseif (G_j(x_{j+1})G_j(x_{j-1}) ≤ 0 and |G_j(x_j)| ≤ h min(|G_j(x_{j-1})|, |G_j(x_{j+1})|)/ave
    and 0 ≤ min(G'_j(x_{j-1})G'_j(x_j), G'_j(x_{j+1})G'_j(x_j)) and |G'_j(x_{j+1})| < |G'_j(x_{j+1})|
    and |G'_j(x_{j-1})| < |G'_j(x_{j-1})|) then
    there is a delta at x_j
    nn = 1
  endif
endif
if (nn ≠ 1 and (h^{1/2}dce4(j) > dne4(j) or h^{1/2}dce5(j) > dne5(j)
or h^{1/2}dci4(j) > dni4(j) or h^{1/2}dci5(j) > dni5(j)
or h^{1/2}dce4(j-1) > dne4(j-1) or h^{1/2}dce5(j-1) > dne5(j-1))) then
  if (G'_j(x_j)G'_j(x_{j-1}) < 0 and min(|G'_j(x_{j-1})|, |G'_j(x_j)|) ≥ h^2
    and 0 ≤ min(G''_j(x_{j-1})G''_j(x_j), G''_j(x_{j+1})G''_j(x_j)) and |G'_j(x_j)| < |G''_j(x_j)|
    and |G'_j(x_{j-1})| < |G''_j(x_{j-1})|) then
    there is a jump in (x_{j-1}, x_j)
  elseif (G''_j(x_j)G''_j(x_{j-1}) < 0 and min(|G''_j(x_{j-1})|, |G''_j(x_j)|) ≥ h^2
    and 0 ≤ min(G'_j(x_{j-1})G'_j(x_j), G'_j(x_{j+1})G'_j(x_j)) and |G'_j(x_j)| < |G''_j(x_j)|
    and |G'_j(x_{j-1})| < |G''_j(x_{j-1})|) then
    there is a corner in (x_{j-1}, x_j)
  elseif (G_j(x_j)G_j(x_{j-1}) < 0 and min(|G_j(x_{j-1})|, |G_j(x_{j+1})|) ≥ h^2ave
    and 0 ≤ min(G'_j(x_{j-1})G'_j(x_j), G'_j(x_{j+1})G'_j(x_j)) and |G'_j(x_j)| < |G'_j(x_j)|
    and |G'_j(x_{j-1})| < |G'_j(x_{j-1})|) then
    there is a delta in (x_{j-1}, x_j)
  endif
endif

```

FIG. A.1. Algorithm to detect weak singularities.

same happens with the other conditions for other singularities (see Tables 7.8 and 7.9 and Figure A.1)

Our strategy to detect weak singularities is summarized in Figure A.1.

Remark A.1. We have seen in section 4 that $G_j(x)$ can be expressed directly in terms of the sampled data $\mathcal{D}f$. Thus, these conditions can be checked without explicit knowledge of $\tilde{D}H$. We must note that the derivation of G_j in terms of $\mathcal{D}f$ explicitly assumes that $\mathcal{S}_{j-1} \cap \mathcal{S}_{j+1} = \emptyset$. Regardless of the outcome of Algorithm I for these two stencils, when using G_j to confirm the presence of a singularity we always (as we should) use stencils that do not cross the singularity.

Remark A.2. The use of “ave” in Figure A.1 helps in localizing “small” deltas. The size of the jumps and corners is assumed to be $O(1)$.

If a singularity is confirmed at a particular location, we proceed as follows: If the singularity is located in (x_{j-1}, x_j) , we apply the SR technique. We must also check the stencils in the neighboring polynomial pieces to make sure that the accuracy is maintained (they do not cross the singularity). We should then have

$$i(j-1) = j-r-1, \quad i(j+1) = j+1,$$

and we use Algorithm II to determine \mathcal{S}_{j-2} and \mathcal{S}_{j+2} . It can be proven (using Taylor expansions) that the stencils obtained with Algorithm I for intervals further away from the singularity do not cross it, i.e., $i(j+n) \geq j+1$ and $i(j-n) \leq j-r+1$ for $n = 3, 4, \dots$ as long as we are far enough from other singularities.

If the singularity is located at the grid point x_j , it is sufficient to modify the neighboring stencils (no SR is needed). We take

$$i(j) = j-r, \quad i(j+1) = j+1,$$

and use Algorithm II to determine $i(j-1)$ and $i(j+2)$. It can also be proven that \mathcal{S}_{j+n} and \mathcal{S}_{j-n+1} do not cross the singularity for $n \geq 3$, as long as we are far enough from other singularities.

REFERENCES

- [1] R. ABGRALL, *Design of an Essentially Nonoscillatory Reconstruction Procedure on Finite Element Type Meshes*, ICASE Report 91-84, 1991; revised INRIA report 1592, 1992.
- [2] F. ARÀNDIGA, R. DONAT, AND A. HARTEN, *Multiresolution based on weighted averages of the hat function I: Linear reconstruction operators*, SIAM J. Numer. Anal., 36 (1998), pp. 160–203.
- [3] A. COHEN, I. DAUBECHIES, AND J. C. FEAUVEAU, *Biorthogonal bases of compactly supported wavelets*, Comm. Pure Appl. Math., 45 (1992), pp. 485–560.
- [4] R. DONAT, *Studies on error propagation for certain nonlinear approximations to hyperbolic equations: Discontinuities in derivatives*, SIAM J. Numer. Anal., 31 (1994), pp. 655–679.
- [5] R. DONAT AND A. HARTEN, *Data Compression Algorithms for Locally Oscillatory Data*, UCLA CAM Report 93-26, Univ. of California, Los Angeles, CA, 1993.
- [6] A. HARTEN, *ENO schemes with subcell resolution*, J. Comput. Phys., 83 (1989), pp. 148–184.
- [7] A. HARTEN, *Discrete multiresolution analysis and generalized wavelets*, J. Appl. Numer. Math., 12 (1993), pp. 153–192.
- [8] A. HARTEN, *Multiresolution Representation of Data*, UCLA CAM Report 93-13, Univ. of California, Los Angeles, CA, 1993.
- [9] A. HARTEN, *Multiresolution representation of data: General framework*, SIAM J. Numer. Anal., 33 (1996), pp. 1205–1256.
- [10] A. HARTEN, *Multiresolution representation of cell-averaged data*, UCLA CAM Report 94-21, Univ. of California, Los Angeles, CA, 1994.
- [11] A. HARTEN, *Multiresolution algorithms for the numerical solution of hyperbolic Conservation laws*, Comm. Pure Appl. Math., 48 (1995), pp. 1305–1342.
- [12] A. HARTEN, B. ENGQUIST, S. OSHER, AND S. CHAKRAVARTHY, *Uniformly high order accurate essentially non-oscillatory schemes III*, J. Comput. Phys., 71 (1987), pp. 231–303.
- [13] A. HARTEN AND S. CHAKRAVARTHY, *Multi-dimensional ENO Schemes for General Geometries*, ICASE Report 91-76, 1991.